ELSEVIER

International Journal of Solids and Structures 41 (2004) 1081–1118

INTERNATIONAL JOURNAL OF SOLIDS and STRUCTURES

www.elsevier.com/locate/ijsolstr

Stress-intensity factors for surface cracks in functionally graded materials under mode-I thermomechanical loading

Matthew C. Walters, Glaucio H. Paulino, Robert H. Dodds Jr. *

Department of Civil and Environmental Engineering, University of Illinois at Urbana-Champaign, Newmark Civil Engineering Laboratory, 205 North Mathews Avenue, Urbana, IL 61801-2397, USA

Received 14 November 2002; received in revised form 13 September 2003

Abstract

This paper describes the development and application of a general domain integral method to obtain J-values along crack fronts in three-dimensional configurations of isotropic, functionally graded materials (FGMs). The present work considers mode-I, linear-elastic response of cracked specimens subjected to thermomechanical loading, although the domain integral formulation accommodates elastic–plastic behavior in FGMs. Finite element solutions and domain integral J-values for a two-dimensional edge crack show good agreement with available analytical solutions for both tension loading and temperature gradients. A displacement correlation technique provides pointwise stress-intensity values along semi-elliptical surface cracks in FGMs for comparison with values derived from the proposed domain integral. Numerical implementation and mesh refinement issues to maintain path independent J-values are explored. The paper concludes with a parametric study that provides a set of stress-intensity factors for semi-elliptical surface cracks covering a practical range of crack sizes, aspect ratios and material property gradations under tension, bending and spatially-varying temperature loads.

Keywords: Domain integral; Functionally graded material; J-integral; Mode-I stress-intensity factor; Semi-elliptical surface crack; Three dimensions

1. Introduction

In structures composed of functionally graded materials (FGMs), the spatial variation of thermal and mechanical properties influences strongly the response to loading (see Miyamoto et al., 1999, for a general discussion). The presence of a functionally graded interface between two dissimilar materials, for example, can lead to a relaxation in stresses associated with discontinuities at bi-material interfaces (Hasselman and Youngblood, 1978; Lee and Erdogan, 1995; Ravichandran, 1995; Noda, 1999; Nomura et al., 2001).

* Corresponding author. Tel.: +1-217-333-3276; fax: +1-217-333-9464.
E-mail address: r-dodds@uiuc.edu (R.H. Dodds Jr.).

0020-7683/$ - see front matter © 2003 Elsevier Ltd. All rights reserved.
doi:10.1016/j.ijsolstr.2003.09.050

Because fracture remains a key failure mode of FGMs, successful application of these materials depends upon an understanding of their fracture mechanics.

Eischen (1987) and Jin and Noda (1994) demonstrated the correspondence between near-tip fields in homogeneous and nonhomogeneous bodies, which permits the application of standard analysis techniques to cracks in FGMs. Delamination and cracking of FGMs at coating/substrate interfaces due to thermal loads are the focus of investigations by Lee and Erdogan (1995), Bao and Cai (1997), Lee and Erdogan (1998), Quian et al. (1998), and Gaudette et al. (2001). Takahashi et al. (1993) and Fujimoto and Noda (2000, 2001) examine the influence of material gradation and thermal shock on crack propagation. Ravichandran (1995), Jin and Batra (1996), Cai and Bao (1998), and Jin and Batra (1998), discuss residual stresses, crack bridging, residual strength, fracture toughness and *R*-curve behavior. The edge crack in a graded semi-infinite strip under thermal and mechanical loads is a case studied by Erdogan and Wu (1996), Erdogan and Wu (1997), Gu and Asaro (1997), Noda (1997), and Noda and Jin (1993).

Analytical and numerical studies of fracture in FGMs reported in the literature focus primarily on plane stress, plane strain and axisymmetric configurations (Delale and Erdogan, 1983; Eischen, 1987; Konda and Erdogan, 1994; Dag et al., 1999; Li et al., 1999; Selvadurai, 2000). As understanding of the micromechanical behavior of crack growth in FGMs progresses, computational techniques enable the analysis of realistic configurations in three-dimensions for which analytical solutions do not exist. This work discusses a formulation of the *J*-integral (Rice, 1968) for three-dimensional (3-D) models of FGMs with numerical implementation using a domain integral approach. Applications focus on semi-elliptical surface cracks that have received much attention for homogeneous materials, and that represent a common failure mechanism in brittle materials and FGMs (Bahr et al., 1986; Kawasaki and Watanabe, 1993; Takahashi et al., 1993; Kokini et al., 1996).

Techniques to obtain stress-intensity factors in components made of homogeneous and nonhomogeneous materials include the displacement correlation technique (DCT) (Shih et al., 1976; Kim and Paulino, 2002a), the modified crack-closure integral (Rybicki and Kanninen, 1977; Kim and Paulino, 2002b), the interaction integral (Yau et al., 1980) and stress correlation (Raju and Newman, 1979). For nonlinear behavior, the domain-integral technique (Li et al., 1985) based on the *J*-integral (Rice, 1968) remains (strictly) valid for deformation plasticity and approximately valid for incremental plasticity. The current study considers only linear-elastic behavior.

The next section examines the finite element analysis of uncracked bodies with smoothly-graded material properties under thermomechanical loads, and verifies the numerical techniques by comparison with published analytical solutions. A general, and numerically convenient, formulation of the domain integral for nonhomogeneous materials and quasi-static thermomechanical loads is then developed, followed by a description of the numerical evaluation in a finite-element setting. The literature provides examples to verify this technique for two-dimensional (2-D) geometries, and the DCT confirms new stress-intensity factors derived here using the *J*-integral approach for 3-D configurations. The paper includes an initial parametric study and discussion of K_I-values calculated for a number of semi-elliptical, surface-crack geometries in functionally-graded plates under mode-I tension, bending and thermal loads. Some final remarks and observations conclude the study.

2. Finite element analysis including graded material properties

With the finite element method, material properties can vary between elements or between integration points. The term *homogeneous element* here describes an element with all integration points assigned a common property value; the term *graded element* here describes an element with integration points that may have different property values. Many researchers, including Williamson and Rabin (1992), Lee and Erdogan (1995), Anlas et al. (2000), Li et al. (2000), Santare and Lambros (2000), Bruck and Gershon

(2002), and Kim and Paulino (2002c) apply homogeneous and graded elements to model uncracked FGMs. With increasing mesh refinement, solutions generated with homogeneous and graded elements converge at a rate dependent upon the severity of material gradients and the quadrature schemes (Kim and Paulino, 2002c). In addition to the zero-energy modes and shear-locking mechanisms associated with homogeneous elements (Bicanic and Hinton, 1979; Kim et al., 1990; Cook et al., 2002), property variation between integration points may introduce additional sources of poor element behavior. For example, with full (four-point) integration, spurious shear strains develop in a four-noded (bilinear) quadrilateral element under a pure tension loading which acts perpendicular to a gradation in elastic modulus. This study employs tri-quadratic (20-noded brick) elements with graded material properties and reduced ($2\times2\times2$) integration—a combination shown here to yield good behavior.

Within graded elements, the calculation of stiffness, stress and other quantities requires the value of properties at integration points. One technique to assign a spatially-varying property at integration points employs temperature-dependent material properties. For example, we may define Young's modulus, $E(\boldsymbol{x})$, $\boldsymbol{x} = (x_1, x_2, x_3)$, as a function of temperature, and then define temperature as a function of spatial position such that the expression $\partial E(\boldsymbol{x})/\partial T(\boldsymbol{x}) \times \partial T(\boldsymbol{x})/\partial x_i$ yields the desired value for $\partial E(\boldsymbol{x})/\partial x_i$. The assignment of a zero thermal expansion coefficient then eliminates unwanted thermal strains. Rousseau and Tippur (2001) adopt this approach which is useful to verify other implementations including those described below. This method permits only one form of spatial variation, $\partial T(\boldsymbol{x})/\partial x_i$, and is not suitable for thermomechanical analyses where temperatures and material properties vary distinctly. The current study employs a more general procedure.

To support multiple material gradients and simultaneous thermal and mechanical loads, element-level routines can retrieve analyst-defined values of material properties at integration points or model nodes. An explicit function that defines the spatial material variation (Konda and Erdogan, 1994), or a routine that calculates properties according to a micromechanical model (Nemat-Nasser and Hori, 1993) are two commonly-used methods to produce the required property values. With analyst-specified nodal values for the properties, interpolation using element shape functions determines property values at integration points. For its generality and accuracy (Li et al., 2000; Kim and Paulino, 2002c), the current study employs the nodal-values approach.

2.1. Performance of graded 3-D elements

This section examines the accuracy of finite-element procedures for the analysis of uncracked bodies with graded elastic moduli and graded coefficients of thermal expansion (CTE). Simple boundary-value problems for 2-D (plane-strain) graded solids that have analytical solutions available in the literature provide benchmarks to assess the performance of the finite element analyses. To simulate plane-strain conditions, the finite-element models described in this section have one layer of 20-noded bricks in the thickness direction, and have out-of-plane displacements constrained to zero. Erdogan and Wu (1997) derive semi-analytical solutions for stresses in an uncracked, semi-infinite graded strip (Fig. 1) subjected to fixed-grip displacement, tension and bending loads. The strip has an exponential variation of Young's modulus in the form $E(x) = E_1 e^{\beta x}$. The constant of material nonhomogeneity, β, follows the relation

$$\beta = \frac{1}{W} \ln\left(\frac{E_2}{E_1}\right), \tag{1}$$

where W denotes the specimen width and E_2/E_1 is the ratio of Young's modulus at $x = W$ and 0. Notice that $1/\beta$ represents the length scale of material nonhomogeneity. Poisson's ratio, ν, remains constant throughout the specimen. In the semi-infinite strip, the plane-strain stress σ_{yy} due to a remotely applied axial force, N, is (Erdogan and Wu, 1997)

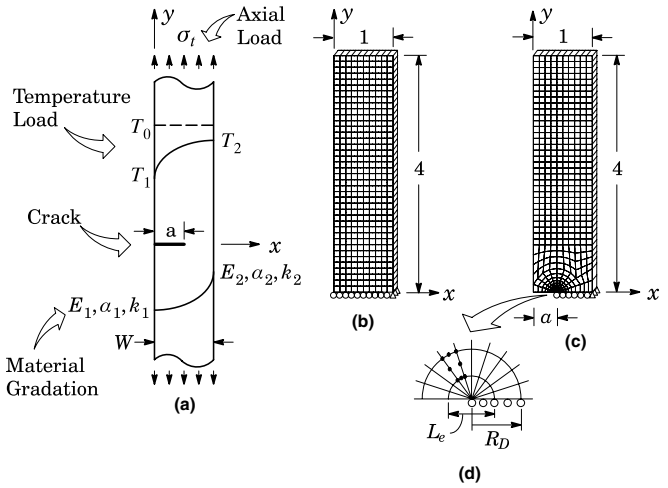

Fig. 1. (a) Schematic of a semi-infinite strip of width W, with material properties graded exponentially in the x-direction. Poisson's ratio, v, is constant, and E_i, a_i, and k_i, $i = 1, 2$, are the Young's moduli, coefficient of thermal expansion, and coefficient of heat conduction at $x = 0$ and W, respectively. The two load cases are: (1) an imposed, uniform axial stress, and (2) an imposed temperature field, with $T(x = 0) = T_1 = 0.05T_0$ and $T(x = W) = T_2 = 0.5T_0$. (b) $40 \times 10 \times 1$ mesh of the uncracked strip ($a = 0$) consisting of 20-noded brick elements. (c) Mesh for the cracked strip: $a/W = 0.4$. (d) Crack-front elements with quarter-point midside nodes and collapsed faces. Dimension R_D provides a measure of domain size, and L_e indicates the size of crack-front elements.

$$\sigma_{yy}(x) = E_0 e^{\beta x}(Ax + B), \tag{2}$$

where values of A and B follow by enforcing the boundary conditions for axial force N and moment M:

$$\int_0^W \sigma_{yy}(x)\,\mathrm{d}x = N \quad \text{and} \quad \int_0^W \sigma_{yy}(x)x\,\mathrm{d}x = M = \frac{NW}{2}. \tag{3}$$

Fig. 2(a) shows $\sigma_{yy}(x)$ on each $y =$ constant section of the strip given by Eq. (2). This curve corresponds to the ratio $E_2/E_1 = 10$, with normalization by the applied stress, σ_t. The symbols indicate finite-element stresses at integration points along a constant y-value. They agree very well with the semi-analytical solution. Fig. 2(b) shows the computed deformation of the finite-element model under tension loading.

Erdogan and Wu (1996) also determine the stress distribution in a functionally-graded, semi-infinite strip subjected to thermal loading. They adopt an exponentially-varying Young's modulus and constant Poisson's ratio. For the thermal properties, they also adopt exponentially-varying coefficients of thermal expansion, $\alpha(x) = \alpha_1 e^{\omega x}$, and heat conduction, $k(x) = k_1 e^{\eta x}$, where α_1 and k_1 denote the values of the coefficients at $x = 0$. Here, ω and η set the material nonhomogeneity according to

$$\omega = \frac{1}{W}\ln\left(\frac{\alpha_2}{\alpha_1}\right) \quad \text{and} \quad \eta = \frac{1}{W}\ln\left(\frac{k_2}{k_1}\right). \tag{4}$$

Accordingly, $1/\omega$ and $1/\eta$ represent the length scales of material nonhomogeneity associated with thermal expansion and conductivity, respectively. The temperature distribution follows by solution of the one-dimensional (1-D), steady-state diffusion equation with spatially-dependent conductivity, i.e.

$$\frac{\partial}{\partial x}\left(k(x)\frac{\partial T}{\partial x}\right) = 0, \tag{5}$$

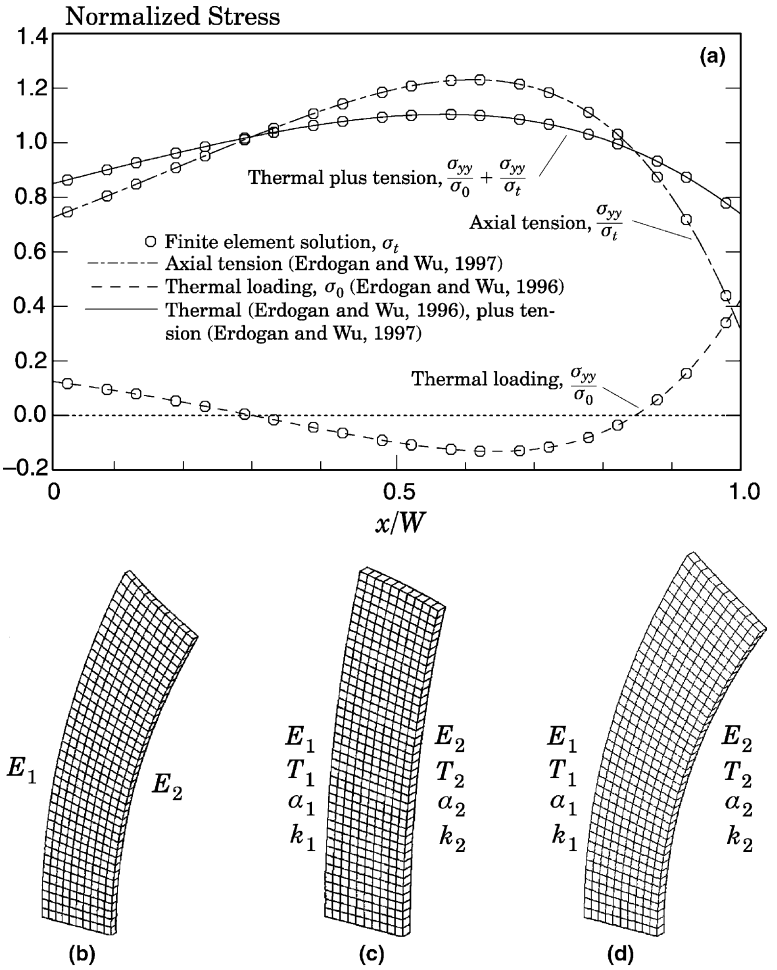

Fig. 2. (a) Analytical and finite-element solutions for $\sigma_{yy}(x)$ in an uncracked semi-infinite strip (shown in Fig. 1) under axial tension loading, steady-state thermal loading, and combined (thermal plus tension) loading, with $E_2/E_1 = 10$, $\alpha_2/\alpha_1 = 2$, $k_2/k_1 = 10$, $T(x = 0) = T_1 = 0.05T_0$ and $T(x = W) = T_2 = 0.5T_0$. (b) Deformed shape of the graded finite-element strip under tension loading, (c) thermal loading, and (d) combined loading.

which yields

$$T(x) = Ce^{-\eta x} + D, \tag{6}$$

where C and D denote constants of integration found by assigning values for k_2/k_1, $T(x = 0)$ and $T(x = W)$. With the known temperature distribution, Erdogan and Wu (1996) show that the plane-strain stress $\sigma_{yy}(x)$ has the form

$$\sigma_{yy}(x) = \frac{E(x)}{(1-\nu^2)}[Ax + B - (1+\nu)\alpha(x)(T(x) - T_0)]. \tag{7}$$

Values for A and B follow upon application of the boundary conditions requiring, respectively, zero net axial force and zero net moment:

$$\int_0^W \sigma_{yy}(x)\,\mathrm{d}x = 0 \quad \text{and} \quad \int_0^W \sigma_{yy}(x)x\,\mathrm{d}x = 0. \tag{8}$$

Fig. 2(a) shows the semi-analytical and finite-element stresses for this simple thermal loading in a model with the following material properties: $E_2/E_1 = 10$, $\alpha_2/\alpha_1 = 2$, $k_2/k_1 = 10$, $T(x = 0) = T_1 = 0.05T_0$, and $T(x = W) = T_2 = 0.5T_0$ (see Fig. 1). The quantity $\sigma_0 = E_1\alpha_1 T_0/(1 - \nu)$ defines the conventional normalizing stress for thermal loading in plane strain. Fig. 2(c) shows the computed deformation of the finite-element model for the above boundary conditions and material properties.

The semi-analytical solution for the combined tension and thermal loadings superposes the normalized results from Eqs. (2) and (7). The corresponding finite element solution represents one analysis including combined thermal and tension loading (see Fig. 2(a)). Fig. 2(d) shows the deformed shape of the finite-element model under the combined loading. This 2-D example provides a partial verification of the 3-D numerical procedures used in this study to model FGMs.

3. The domain integral for cracks in FGMs

Three-dimensional domain integral methods rely upon volume integrals to compute J-values pointwise along crack fronts. Early works on the domain integral method (Li et al., 1985; Shih et al., 1986; Moran and Shih, 1987a; Nikishkov and Atluri, 1987a; Nikishkov and Atluri, 1987b; Shivakumar and Raju, 1992) formulate the procedure for 2-D (area) and 3-D (volume) domains, and apply the technique to cracks in homogeneous solids under linear-elastic and elastic–plastic deformations arising from mechanical and thermal loads. Gu et al. (1999), Chen et al. (2000), and Kim and Paulino (2002a, 2003) extend the domain-integral method to 2-D FGM specimens under isothermal, linear-elastic loading. The interaction-integral method, based upon the J-integral, is useful to obtain mixed-mode stress-intensity factors in linear-elastic 3-D solids (Nakamura and Parks, 1989). Dolbow and Gosz (2002) apply the interaction integral method to FGM specimens under mechanical loading. These studies of simple 2-D models with through cracks in FGMs determine stress-intensity factors that compare well with analytical values, but none of them investigate 3-D configurations. The following sections describe the formulation of the 3-D domain integral for FGMs.

3.1. The 3-D domain integral

The following derivation of the 3-D domain integral parallels those found in Shih et al. (1986) and Moran and Shih (1987b) for homogeneous materials. The pointwise energy release rate along a generally-curved, planar crack-front in 3-D has the form

$$J(s) = \lim_{\Gamma \to 0} \int_{\Gamma} (W\delta_{1i} - \sigma_{ij}u_{j,1})n_i \, \mathrm{d}C, \tag{9}$$

where W is strain energy density, σ_{ij} denotes stress, u_j represents displacement, and $(\cdot)_{,i} = \partial(\cdot)/\partial X_i$, where X_i refers to local coordinates defined at each point, s, along a crack front. Fig. 3 illustrates the local coordinate system at location s, where X_2 is normal to the crack plane, X_3 defines the in-plane tangent to the crack, and X_1 defines the in-plane normal. The curve Γ encloses the crack-front in the X_1–X_2 plane. As written, Eq. (9) remains valid for nonlinear-elastic material behavior, and equals the standard J-integral (Rice, 1968) including effects of body forces, crack-face tractions, thermal strains and general material property gradation only when $r \to 0^+$.

In global coordinates, x_i, let $v_k(s)$ be defined as the unit normal to the crack-front at position s, lying in the X_1–X_3 plane. Eq. (9) then represents the first component of the vector integral

$$J(s) = J_k(s)v_k(s) = \lim_{\Gamma \to 0} \int_{\Gamma} (\sigma_{ij}u_{j,k} - W\delta_{ik})m_i v_k \, \mathrm{d}C, \tag{10}$$

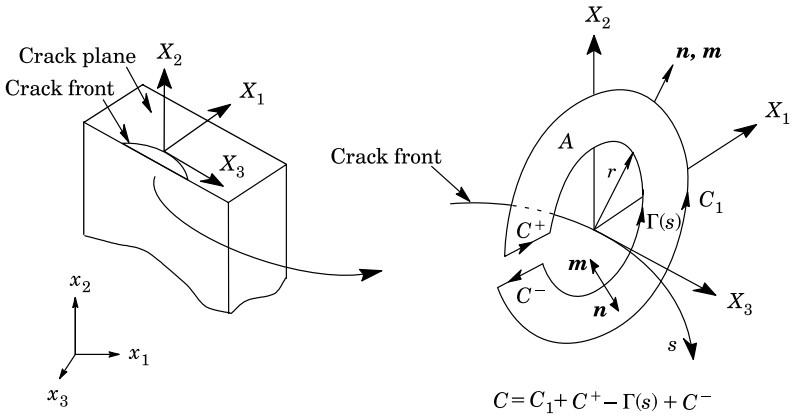

Fig. 3. Schematic of $\Gamma(s)$ in Eq. (9). The domain for the analogous 2-D integral is the area A, bounded by the contour $C = C_1 + C^+ - \Gamma(s) + C^-$.

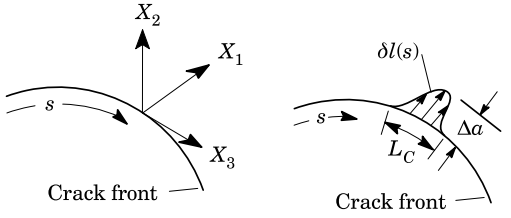

Fig. 4. (after Shih et al., 1986) Virtual crack advance in the local X_1–X_3 plane at crack-front location s. Crack advance occurs in the X_1-direction, and is defined as $\delta l(s) = \Delta a l_k(s) v_k(s)$.

where $m_i = -n_i$ on $\Gamma(s)$ as shown in Fig. 3. A virtual displacement applied to a segment of the crack-front takes the form

$$\delta l(s) = \Delta a l_k(s) v_k(s), \tag{11}$$

as illustrated in Fig. 4. Here, Δa is the amplitude of the arbitrary displacement, l_k. A first-order approximation of the energy released due to the crack advance, $-\delta\pi$, is (Rice et al., 1973)

$$-\delta\pi = \int_{L_C} J(s)\delta l(s)\,\mathrm{d}s, \tag{12}$$

where L_C refers to a finite segment of the crack-front, as illustrated in Figs. 4 and 5. Eqs. (11) and (12) together give

$$-\delta\pi = \overline{J}\Delta a = \Delta a \int_{L_C} J(s) l_k(s) v_k(s)\,\mathrm{d}s, \tag{13}$$

where $\overline{J}$ represents the energy released when crack segment L_C advances by $\delta l(s)$. By combining Eqs. (10) and (13), one obtains

$$\overline{J}\Delta a = \Delta a \int_{L_C} l_k(s) \left[\lim_{\Gamma \to 0} \int_{\Gamma} (\sigma_{ij} u_{j,k} - W\delta_{ik}) m_i \,\mathrm{d}C \right] \mathrm{d}s \tag{14}$$

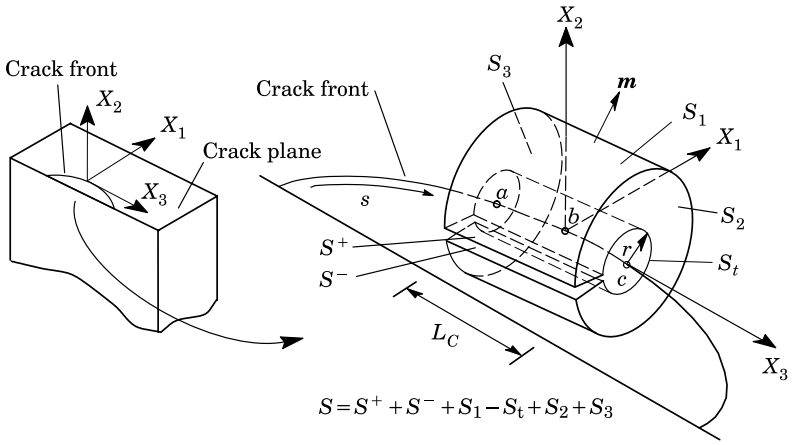

Fig. 5. Surface and volume domains used to calculate $J(s)$ at crack-front location $s = b$ extend from point a to point c, a length equal to L_C. Surfaces S_t and S_1 (cylindrical surfaces), S_2 and S_3 (flat lateral surfaces), and S^+, and S^- (top and bottom crack-face surfaces) comprise surface S and enclose volume V of the domain integral. For general loading conditions, S_t must shrink to the crack tip, i.e. $r \to 0^+$. Vector $\boldsymbol{m}$ is the outward normal to S_t, S_1, S^+, and S^-.

$$\overline{J}\Delta a = \Delta a \lim_{\Gamma \to 0} \int_{S_t} (\sigma_{ij} u_{j,k} - W\delta_{ik}) l_k m_i \, \mathrm{d}S, \tag{15}$$

where S_t, shown in Fig. 5, is the surface created by "extruding" $\Gamma(s)$ in Fig. 3 over a distance L_C along the crack front. The radius of this surface shrinks to the crack-front in the limiting process. The divergence of the integrand in Eq. (15) is zero for the same conditions that guarantee path independence of the 2-D J-integral, i.e. quasi-static, isothermal loading, elastic constitutive behavior, and no body forces or inertia. In the presence of general loading conditions, the integrand is not divergence free, and takes the form

$$\left(\sigma_{ij} u_{j,k} - W\delta_{ik}\right)_{,i} = \left(\sigma_{ij,i} u_{j,k} + \sigma_{ij} u_{j,ki} - W_{,k}\right). \tag{16}$$

In this expression, the definition of strain energy density, W, includes the effects of thermal strains, non-linear (elastic) deformation and material gradients, as discussed in a following section. The present goal is to obtain a volume integral equivalent to Eq. (15). To accomplish this, we multiply both sides of Eq. (16) by an arbitrary, sufficiently smooth vector field q_k, and integrate over any simply connected region V within the loaded body to obtain

$$\int_V (\sigma_{ij} u_{j,k} - W\delta_{ki})_{,i} \, q_k \, \mathrm{d}V = \int_V (\sigma_{ij} u_{j,ki} - W_{,k}) q_k \, \mathrm{d}V, \tag{17}$$

where the present assumption of zero body forces and inertia causes $\sigma_{ij,i}\ u_{j,k}$ to vanish. An alternative expression for the left side of Eq. (17) is

$$\int_V (\sigma_{ij} u_{j,k} - W\delta_{ki})_{,i} \, q_k \, \mathrm{d}V = \int_V \left[(\sigma_{ij} u_{j,k} - W\delta_{ki}) q_k\right]_{,i} \mathrm{d}V - \int_V (\sigma_{ij} u_{j,k} - W\delta_{ki}) q_{k,i} \, \mathrm{d}V. \tag{18}$$

A surface integral results from applying the divergence theorem to the first integral on the right side of Eq. (18). An expression for this surface integral follows from Eqs. (17) and (18):

$$\int_S (\sigma_{ij} u_{j,k} - W\delta_{ki}) q_k m_i \, \mathrm{d}S = \int_V (\sigma_{ij} u_{j,k} - W\delta_{ki}) q_{k,i} \, \mathrm{d}V + \int_V (\sigma_{ij} u_{j,ki} - W_{,k}) q_k \, \mathrm{d}V. \tag{19}$$

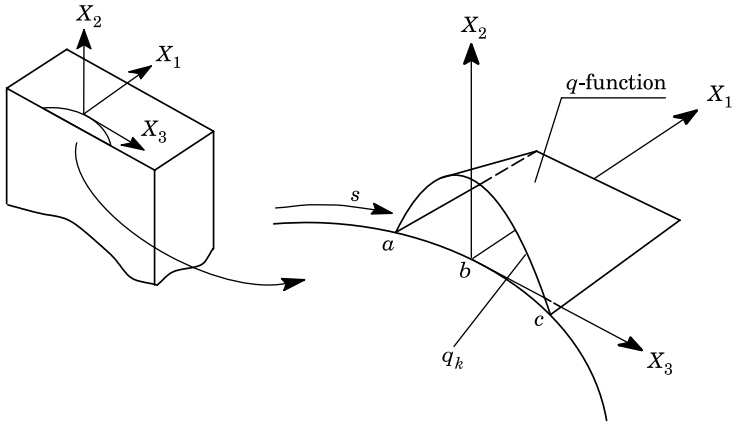

Fig. 6. The arbitrary function q_k is interpreted as a virtual crack-front displacement, and varies from unity on surface S_t at location $s = b$, to zero on surfaces S_1, S_2 and S_3 (see Fig. 5).

Because surface S of the above surface integral encloses an arbitrary volume V, a suitable definition is $S = S^+ + S^- + S_1 - S_t + S_2 + S_3$ (see Fig. 5). The arbitrary function q_k varies smoothly within V as follows (Shih et al., 1986):

$$q_k = \begin{cases} l_k & \text{on } S_t, \\ 0 & \text{on } S_1, S_2, S_3, \\ \text{arbitrary elsewhere.} \end{cases} \tag{20}$$

Fig. 6 illustrates schematically a permissible definition of q_k. According to this definition of S and q_k, the right-hand side of Eq. (19) equals the integral in Eq. (15), and one may write

$$\overline{J} = \int_V \left(\sigma_{ij} u_{j,k} - W\delta_{ki}\right) q_{k,i}\, \mathrm{d}V + \int_V \left(\sigma_{ij} u_{j,ki} - W_{,k}\right) q_k\, \mathrm{d}V, \tag{21}$$

when body forces, inertia and crack-face tractions are absent. As mentioned previously, the second integrand in this expression vanishes for a homogeneous body under isothermal, quasi-static loading and elastic material behavior.

By assuming that the energy release rate varies little over the length, L_C, of the domain under consideration, $J(s)$ may be moved outside the integrand in Eq. (13). Eqs. (13) and (21) then combine to yield an expression for the pointwise value of $J(s)$:

$$J(s) = \frac{\overline{J}}{\int_{L_C} l_k(s) v_k(s)\, \mathrm{d}s}. \tag{22}$$

The transformation of stresses and displacements to the crack-front coordinate system (X_i in Figs. 3–6) simplifies the form of Eq. (21). In this case, $v_k(s) = X_1(s)$, and all subscripts "k" in Eqs. (21) and (22) become "1." The discussion below adopts this approach to evaluate $J(s)$.

3.2. Derivative of strain energy density: $W_{,1}$

The strain energy density, W, can be defined as a function of the total strain ε^t_{ij}, temperature Θ, and spatial position $\boldsymbol{x} = (x_1, x_2, x_3)$:

$$W(\varepsilon_{ij}^t, \Theta, \boldsymbol{x}) = \int_0^{\varepsilon_{kl}^m} \sigma_{ij}\, \mathrm{d}\varepsilon_{ij}^m, \tag{23}$$

where for uncoupled, quasi-static thermomechanical analysis, mechanical strains, ε_{ij}^m, equal total strains, ε_{ij}^t, minus thermal strains, ε_{ij}^{th}:

$$\varepsilon_{ij}^m = \varepsilon_{ij}^t - \varepsilon_{ij}^{th} = \varepsilon_{ij}^t - \alpha(\boldsymbol{x})\Theta(\boldsymbol{x})\delta_{ij}. \tag{24}$$

Here, $\alpha(\boldsymbol{x})$ is the pointwise-isotropic coefficient of thermal expansion, $\Theta(\boldsymbol{x})$ is the relative change in temperature, and δ_{ij} represents the Kronecker delta. The derivative of strain energy density, $W_{,1}$, needed to evaluate Eq. (21), becomes

$$W_{,1} = \frac{\partial W}{\partial \varepsilon_{ij}^m}\varepsilon_{ij,1}^m + (W_{,1})_{\text{explicit}}, \tag{25}$$

which, combined with Eq. (24), yields

$$W_{,1} = \sigma_{ij}(\varepsilon_{ij}^t - \varepsilon_{ij}^{th})_{,1} + (W_{,1})_{\text{explicit}} \tag{26}$$

$$= \sigma_{ij}(\varepsilon_{ij,1}^t - \alpha_{,1}(\boldsymbol{x})\Theta(\boldsymbol{x})\delta_{ij} - \alpha(\boldsymbol{x})\Theta_{,1}(\boldsymbol{x})\delta_{ij}) + (W_{,1})_{\text{explicit}}, \tag{27}$$

where $(W_{,1})_{\text{explicit}}$ denotes the derivative of strain energy density with respect to spatially-dependent parameters. Substitution of Eq. (27) into Eq. (21) causes $\sigma_{ij}u_{j,1i}$ to cancel with $\sigma_{ij}\varepsilon_{ij,1}^t$ and the result is

$$\overline{J} = \int_V (\sigma_{ij}u_{j,1} - W\delta_{1i})q_{1,i}\, \mathrm{d}V + \int_V \left[\sigma_{ij}(\alpha_{,1}(\boldsymbol{x})\Theta(\boldsymbol{x})\delta_{ij} + \alpha(\boldsymbol{x})\Theta_{,1}(\boldsymbol{x})\delta_{ij}) - (W_{,1})_{\text{explicit}}\right] q_1\, \mathrm{d}V. \tag{28}$$

The second integral of (28) represents a *correction* term to account for the nonvanishing divergence of the J-integral in the presence of thermal strains and material property gradients. Terms related to thermal effects are easily calculated from known distributions of CTEs and temperature (Shih et al., 1986). Typically for FGMs, $(W_{,1})_{\text{explicit}}$ derives from a specific definition of strain energy density (Chen et al., 2000; Kim and Paulino, 2002a, 2003). A description of two forms for this term follows in the next section.

3.3. Assessment of alternative forms of $(W_{,1})_{explicit}$

For small displacement gradients in a nonhomogeneous, linear-elastic isotropic material, Eq. (23) becomes

$$W(\varepsilon_{ij}^t, \Theta, \boldsymbol{x}) = \int_0^{\varepsilon_{rs}^m} C_{ijkl}(\boldsymbol{x})\varepsilon_{kl}^m\, \mathrm{d}\varepsilon_{ij}^m, \tag{29}$$

where $C_{ijkl}(\boldsymbol{x})$ is the spatially-varying isotropic elastic constitutive tensor

$$C_{ijkl}(\boldsymbol{x}) = \lambda(\boldsymbol{x})\delta_{ij}\delta_{kl} + \mu(\boldsymbol{x})(\delta_{ik}\delta_{jl} + \delta_{il}\delta_{jk}), \tag{30}$$

in which δ_{ij} is the Kronecker delta, and the spatially-varying Lamé constants $\lambda(\boldsymbol{x})$ amd $\mu(\boldsymbol{x})$ are

$$\lambda(\boldsymbol{x}) = \frac{E(\boldsymbol{x})v(\boldsymbol{x})}{(1+v(\boldsymbol{x}))(1-2v(\boldsymbol{x}))} \quad \text{and} \quad \mu(\boldsymbol{x}) = \frac{E(\boldsymbol{x})}{2(1+v(\boldsymbol{x}))}. \tag{31}$$

$(W_{,1})_{\text{explicit}}$ is

$$(W_{,1})_{\text{explicit}} = \frac{\partial W}{\partial E(\boldsymbol{x})}E_{,1}(\boldsymbol{x}) + \frac{\partial W}{\partial v(\boldsymbol{x})}v_{,1}(\boldsymbol{x}). \tag{32}$$

For homogeneous materials governed by Eq. (29), $(W_{,1})_{\text{explicit}} = 0$, and under isothermal conditions, the second integral of Eq. (28) vanishes completely. In graded materials where $(W_{,1})_{\text{explicit}} \neq 0$, Eq. (29) leads to analytical expressions for $\partial W/\partial E(\boldsymbol{x})$ and $\partial W/\partial v(\boldsymbol{x})$. For material variations expressed by smooth analytical functions, e.g. $E(\boldsymbol{x}) = E_1 e^{\beta x_1}$, the evaluation of $E_{,1}(\boldsymbol{x})$ and $v_{,1}(\boldsymbol{x})$ becomes straightforward, e.g. $E_{,1}(\boldsymbol{x}) = \beta E(\boldsymbol{x})$.

Another example of nonzero $(W_{,1})_{\text{explicit}}$ arises when a function such as the Ramberg–Osgood equation describes the multi-axial nonlinear stress–strain relationship: $\varepsilon_{ij} = \varepsilon_m \delta_{ij} + e^e_{ij} + 3/2 \times \alpha(\boldsymbol{x})[\sigma_e/\sigma_0(\boldsymbol{x})]^{n(\boldsymbol{x})-1} \times S_{ij}/E(\boldsymbol{x})$, where ε_m is the mean strain, δ_{ij} the Kronecker delta, ε^e_{ij} the elastic deviator strain, σ_e the equivalent (Mises) stress, $\sigma_0(\boldsymbol{x})$ the yield stress, S_{ij} the deviator stress, $E(\boldsymbol{x})$ the Young's modulus, and $\alpha(\boldsymbol{x})$ and $n(\boldsymbol{x})$ are the spatially-varying scalar parameters. In this case, one expression for strain energy density is

$$W(\varepsilon^t_{ij}, \boldsymbol{x}, \Theta) = \frac{1+v(\boldsymbol{x})}{3E(\boldsymbol{x})}\sigma_e^2 + \frac{3}{2}\frac{1-2v(\boldsymbol{x})}{E(\boldsymbol{x})}p^2 + \frac{\sigma_e^2 n(\boldsymbol{x})}{n(\boldsymbol{x})+1}\frac{\alpha(\boldsymbol{x})}{E(\boldsymbol{x})}\left(\frac{\sigma_e}{\sigma_0(\boldsymbol{x})}\right)^{n(\boldsymbol{x})-1}, \tag{33}$$

where p is the hydrostatic pressure, i.e. $p = -(\sigma_{xx} + \sigma_{yy} + \sigma_{zz})/3$. The explicit derivative $(W_{,1})_{\text{explicit}}$ now becomes difficult to evaluate, i.e.,

$$(W_{,1})_{\text{explicit}} = \frac{\partial W}{\partial E}E_{,1}(\boldsymbol{x}) + \frac{\partial W}{\partial v}v_{,1}(\boldsymbol{x}) + \frac{\partial W}{\partial \alpha}\alpha_{,1}(\boldsymbol{x}) + \frac{\partial W}{\partial n}n_{,1}(\boldsymbol{x}) + \frac{\partial W}{\partial \sigma_0}\sigma_{0,1}(\boldsymbol{x}). \tag{34}$$

These two examples illustrate that although Eq. (23) is quite general, the analytical form of $(W_{,1})_{\text{explicit}}$ is material-specific and likely becomes tedious to evaluate when the "1" direction changes continuously along a 3-D curved crack relative to the property gradient directions.

3.4. A general expression for $(W_{,1})_{\text{explicit}}$

Rearrangement of Eq. (27) provides an expression for $(W_{,1})_{\text{explicit}}$ that leads to more convenient numerical evaluation:

$$(W_{,1})_{\text{explicit}} = W_{,1} - \sigma_{ij}(\varepsilon^t_{ij,1} - \alpha_{,1}(\boldsymbol{x})\Theta(\boldsymbol{x})\delta_{ij} - \alpha(\boldsymbol{x})\Theta_{,1}(\boldsymbol{x})\delta_{ij}). \tag{35}$$

Substitution of this expression into Eq. (28) gives

$$\overline{J} = \int_V (\sigma_{ij}u_{j,1} - W\delta_{1i})q_{1,i}\,\mathrm{d}V + \int_V (\sigma_{ij}\varepsilon^t_{ij,1} - W_{,1})q_1\,\mathrm{d}V, \tag{36}$$

which is equivalent to Eq. (21) since $\sigma_{ij}u_{j,1i} = \sigma_{ij}\varepsilon^t_{ij,1}$. This expression yields $J(s)$ when combined with Eq. (22). This is an expected result because the terms in Eq. (35) are the same as those used to transform Eq. (21) into Eq. (28). Eq. (36) now replaces Eq. (21) for numerical computation, and specifically accounts for the effects of material gradients and thermal strains. The appearance in Eq. (36) of $\sigma_{ij}\varepsilon^t_{ij,1}$ rather than $\sigma_{ij}u_{j,1i}$ follows from the derivation rather than from a deliberate substitution. Both terms include second derivatives of displacement, and provide similar accuracy. Eq. (36) is the three-dimensional equivalent of Eq. (6.7) in Moran and Shih (1987b), which defines J for an elastic–plastic material.

Eq. (36) accounts for material gradients and thermal stresses, but omits other standard terms to account for body forces, inertia and crack-face tractions (c.f. Anderson, 1995). The use of Eq. (36) to calculate J remains valid for nonlinear elasticity (deformation plasticity), and leads to computational generality since all quantities are available from standard finite-element calculations. For analyses using flow-theory constitutive models with parameters that vary spatially, the proposed form of J does not retain strict validity – this is the same issue of computing the ordinary J for incremental-flow theory of plasticity vs. deformation plasticity. Another consideration regarding Eq. (36) is the replacement of analytically-defined derivatives in the second integrand of Eq. (28) by derivatives (including $\varepsilon_{ij,1}$) obtained via potentially less accurate,

mesh-dependent interpolation schemes. For homogeneous materials, Eq. (28) yields greater accuracy than Eq. (36) because $(W_{,1})_{\text{explicit}}$ and $\alpha_{,1}$ vanish and the temperature derivative, $\Theta_{,1}$, is generally quite smooth. The remainder of this study examines the implementation, accuracy and application of Eq. (36) for graded materials under thermomechanical loading.

4. Numerical implementation

Numerical evaluation of the integrals in Eq. (36) uses the same quadrature schemes employed for element stiffness computation. The discretized form of Eq. (36) is

$$\overline{J} = \sum_{\text{elems}} \sum_{p} \left\{ \left[(\sigma_{ij} u_{j,1} - W\delta_{1i}) q_{1,i} + (\sigma_{ij}\varepsilon^t_{ij,1} - W_{,1}) q_1 \right] \det\left(\frac{\partial X_k}{\partial \eta_1} \right) \right\}_p w_p. \tag{37}$$

For the equivalent expression derived from Eq. (28), $[\cdot]$ in Eq. (36) is

$$\left[(\sigma_{ij} u_{j,1} - W\delta_{1i}) q_{1,i} + (\alpha_{,1}(\boldsymbol{x})\Theta(\boldsymbol{x})\delta_{ij} + \alpha(\boldsymbol{x})\Theta_{,1}(\boldsymbol{x})\delta_{ij} - (W_{,1})_{\text{explicit}}) q_1 \right].$$

In both expressions, the outer sum includes all elements in the domain, and the inner sum ranges over each element integration point p with corresponding weight w_p. The determinant of the coordinate Jacobian, $\det(\cdot)$, relates local crack-front coordinates X_k to parent-element coordinates η_k. Computation of spatial derivatives for strain and strain energy density at integration points proceeds as follows:

- Use a standard procedure (e.g. Cook et al., 2002) to extrapolate strains and strain energy density from element integration points to element nodes.
- Average these extrapolated nodal values with contributions from adjoining elements.
- Calculate derivatives at integration points using isoparametric interpolation, i.e.

$$\frac{\partial (\varepsilon^t_{ij})_p}{\partial x_1} = \sum_{I=1}^{n} \sum_{k=1}^{3} \frac{\partial N_I}{\partial \eta_k} \frac{\partial \eta_k}{\partial x_1} (\varepsilon^t_{ij})_I \quad \text{and} \quad \frac{\partial W_p}{\partial x_1} = \sum_{I=1}^{n} \sum_{k=1}^{3} \frac{\partial N_I}{\partial \eta_k} \frac{\partial \eta_k}{\partial x_1} W_I, \tag{38}$$

where $(\varepsilon^t_{ij})_p$ and W_p denote integration point quantities, n is the number of element nodes, N_I is the element shape function corresponding to node I, η_k are parent coordinates, and $(\varepsilon^t_{ij})_I$ and W_I are the nodal values of total strain and strain energy density.

The WARP3D fracture code used for this implementation is a free, open-source, general-purpose finite-element software developed at the University of Illinois at Urbana-Champaign (Gullerud et al., 2000). J-integral results reported here employ Eqs. (37) and (38) with 20-noded isoparametric "brick" elements with reduced $(2\times2\times2)$ integration.

5. Verification of the general J-formulation for 2-D configurations

Erdogan and Wu (1997) describe analytical solutions for a crack located in a semi-infinite strip and subjected to tensile, fixed-grip and bending loads. Fig. 1(c) shows the cracked strip where $a/W = 0.4$, and a group of ten focused (collapsed) elements, shown in Fig. 1(d), surround the crack-front region. This mesh employs quarter-point elements, and coincident crack-front nodes share the same x-displacement, i.e. they have identical node numbers. The ratio of the length, L_e, of crack-front elements on the crack plane to the strip width, W, is $L_e/W = 0.007$ (see Fig. 1(d)). Thirteen semi-circular domains produce J-values in a mesh consisting of 496 20-noded bricks and 3735 nodes. An exponential variation, $E(x) = E_1 e^{\beta x}$, describes the

gradient of Young's modulus, where $E_2/E_1 = 10$, and β follows from Eq. (1). Poisson's ratio remains constant at $v = 0.3$, and constrained out-of-plane displacements enforce plane-strain conditions. Eq. (36) leads to $J(s)$ for an imposed tensile stress σ_t. The conversion of J-values to K_I-values here follows the standard expression

$$K_I(s) = (J(s)E^*(s))^{1/2}, \tag{39}$$

where $E^*(s) = E(s)/(1 - v^2)$ for plane-strain conditions, $E^*(s) = E(s)$ for plane-stress conditions, and $E(s)$ denotes the value of Young's modulus at crack-front location s. The use of $E(s)$ follows from the identical form of the asymptotic crack-front fields in homogeneous and functionally graded materials (Eischen, 1987; Jin and Noda, 1994). For discussion, normalized K_I-values equal

$$K_{In} = \frac{K_I}{\sigma_t\sqrt{\pi a}}, \tag{40}$$

where σ_t is the applied tensile stress, and a is crack depth (see Fig. 1). Table 1 lists K_{In}-values for two different analyses and compares them with those of Erdogan and Wu (1997). The first analysis employs Eq. (36). To avoid the interpolations used to evaluate Eq. (36), the second analysis uses the analytical expression for $(W_{,1})_{\text{explicit}}$ given in Eq. (32), together with Eqs. (21) and (25). In all cases, an average of the J-values from domains three through thirteen is inserted into Eqs. (39) and (40) to define a single K_{In}-value shown in Table 1.

The influence of the two integrals in Eq. (36) becomes apparent in Fig. 7(a), which compares the value of each integral vs. the radius, R_D, shown schematically in Fig. 1(d), of the specific computational domain. With increased domain size, the influence of the second integral increases steadily, and without this term, the J-integral becomes proportionately inaccurate.

Through a two-step perturbation procedure, Erdogan and Wu (1996) obtain K_I-values for a semi-infinite, exponentially-graded, cracked strip subjected to thermal loading (see Fig. 1(a), and Wilson and Yu, 1979). Eqs. (1) and (4) describe the exponential material variation specified for the strip. In the first step of the solution procedure, Erdogan and Wu determine the axial stress distribution, σ_{yy}, in an uncracked, thermally-loaded strip. This stress, shown as the lower curve in Fig. 2(a), represents a crack-closure stress, which, in the second step, produces crack-face tractions acting to drive crack opening in the cracked strip. Integral equations then yield stress-intensity factors generated by these crack-face tractions. Values taken from the graphical results of Erdogan and Wu (1996) enable comparisons with the present finite-element analyses.

In the finite-element analysis procedure used here, thermal loads act directly upon the cracked strip. The mesh used for this analysis, shown in Fig. 7(b), has a height-to-width ratio of four, a crack-length-to-width ratio, a/W, of 0.5, and constrained out-of-plane displacements to enforce plane-strain conditions. As in the previous example, a group of ten focused (collapsed) elements surround the crack-front region, the ratio of crack-front element length, L_e, to strip width, W, is 0.007, and all crack-front nodes have zero y-displacement. This mesh employs quarter-point elements, and coincident crack-front nodes share the same x-displacement, i.e. they have identical node numbers. The mesh consists of 50 820-noded brick elements and 3829 nodes. The following examples employ two material variations and two thermal loading conditions

Table 1
Normalized K_I-values for a plane-strain, semi-infinite strip under axial tension (see Fig. 1): $E_2/E_1 = 10$, $v = 0.3$, $a/W = 0.4$

Analysis	Method	K_{In}	% Diff.
Reference	Erdogan and Wu (1997)	1.588	–
1st	Eq. (36)	1.579	−0.57
2nd	$(W_{,1})_{\text{explicit}}$ Eq. (32)	1.588	+0.00

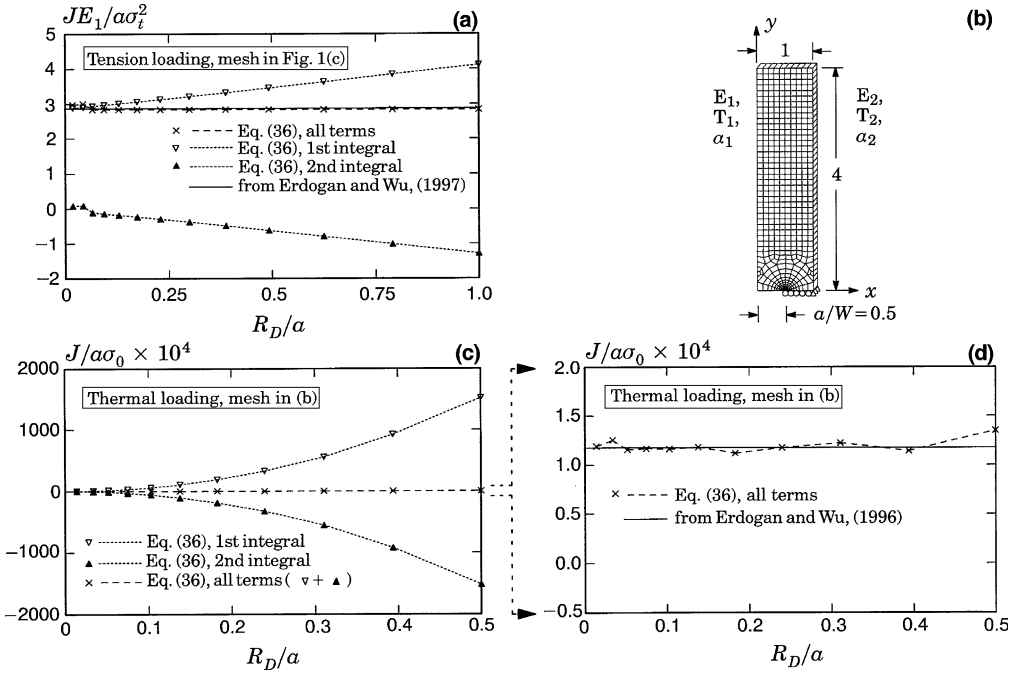

Fig. 7. (a) Normalized components of Eq. (36) for tension loading of SE(T) specimen in Fig. 1(c) for $a/W = 0.4$ and $E_2/E_1 = 10$. (b) Mesh used for thermally-loaded SE(T) specimen: $a/W = 0.5$. (c) Normalized components of Eq. (36) for uniform thermal loading for $T_1 = T_2 = 0.05T_0$, $E_2/E_1 = 5$, and $\alpha_2/\alpha_1 = 2$ ($\sigma_0 = E_1\alpha_1 T_0/(1-\nu)$). (d) Scaled view of data in (c).

selected from Erdogan and Wu (1996) which Table 2 describes. They include the application of two uniform temperature loads to an exponentially-graded strip where $E_2/E_1 = 5$, $\alpha_2/\alpha_1 = 2$, and $\nu = 0.3$, and two exponentially-varying temperature loads to an exponentially-graded strip where $E_2/E_1 = 10$, $k_2/k_1 = 10$, $\alpha_2/\alpha_1 = 2$, and $\nu = 0.3$. A common normalization for K_I-values obtained from thermal loading is

$$K_{In} = \frac{K_I}{E_1'\alpha_1 T_0\sqrt{\pi a}}, \tag{41}$$

Table 2
Normalized K_I-values for a crack in a plane-strain, semi-infinite strip under thermal loads (see Figs. 1(a) and 7(b)): $\nu = 0.3$, $a/W = 0.5$

Material variation	Thermal load (see Fig. 1)	K_{In}		
		Erdogan and Wu (1996)	Eq. (36)	% Diff.
$E_2/E_1 = 5$ $\alpha_2/\alpha_1 = 2$	$T_1 = T_2 = 0.5T_0$	0.0125	0.0127	+1.6
k_2/k_1 is arbitrary	$T_1 = T_2 = 0.05T_0$	0.0245	0.0241	−1.6
$E_2/E_1 = 10$ $\alpha_2/\alpha_1 = 2$	$T_1 = 0.2T_0$ $T_2 = 0.5T_0$	0.0335	0.0335	+0.0
$k_2/k_1 = 10$	$T_1 = 0.05T_0$ $T_2 = 0.5T_0$	0.0410	0.0409	−0.2

where a is crack depth, T_0 is initial temperature, and α_1 is the value of the CTE at the cracked surface. For plane-strain conditions, $E_1' = E_1/(1-\nu)$, and for plane stress conditions, $E_1' = E_1$, where E_1 is the value of Young's modulus at the cracked surface. Table 2 lists stress-intensity factors obtained from each of the four cases and their deviation from the solution obtained from Erdogan and Wu (1996). In each of the four analyses, an average of the J-values from fourteen domains, inserted into Eqs. (39) and (41), leads to a single value of K_{In}.

Fig. 7(c) shows the contribution to J of both integrals in Eq. (36). Both integrals show strong path dependence with an increase in domain size to crack length ratio, R_D/a (see Fig. 1(d)). Because inhomogeneity in both elastic properties and thermal expansion coefficients contribute to J, the path dependence is more severe than for the mechanical loading studied above. Fig. 7(d) shows values of Eq. (36) with an enhanced scale. The J-values for both mechanical and thermal loading show good domain independence.

6. Calculation of mode-I K_I-values for surface cracks

Procedures for obtaining K_I-values for 3-D cracks include the line-spring method (Rice and Levy, 1972), the modified crack-closure integral (MCCI) (Rybicki and Kanninen, 1977; Ramamurthy et al., 1986; Raju, 1987; Narayana et al., 1994), the displacement correlation technique (DCT) (Shih et al., 1976), stress correlation (Raju and Newman, 1979), the domain integral technique (Shih et al., 1986), the interaction integral method (Nakamura and Parks, 1989), and the F-integral (Eriksson, 2002).

Raju and Newman (1979) and Newman and Raju (1979) apply the force method to surface cracks in homogeneous plates under tension and bending loads. Although more recent works report stress-intensity factors for surface cracks (e.g. Rajaram et al., 2000; Ayhan and Nied, 2002), the extensive solutions of Newman and Raju remain a frequently-cited benchmark. For homogeneous materials, the current study uses their results to verify mesh-refinement levels.

The methods listed above also apply to the analysis of FGMs (e.g. Kim and Paulino, 2002a). The MCCI, DCT and stress correlation methods are particularly useful for linear-elastic analyses of FGMs because the presence of material gradients does not influence their formulation. Erdogan and Wu (1997) suggest that the line-spring method, combined with their semi-analytical solutions for the graded 2-D strip discussed in Section 5, provides an approach for the calculation of stress-intensity factors in FGMs with surface cracks. The current study employs the DCT to verify K_I-values obtained through Eq. (36).

6.1. Crack geometries, material variations and loadings

Fig. 8(a) illustrates a plate with a semi-elliptical surface crack under tension, bending and thermal loads. Material properties vary only in the thickness (x) direction. The geometry, loading and material property variations lead to mode-I conditions on the crack plane. Symmetry permits modelling of only one quarter of the specimen. Variables of interest in this study include: crack depth, a; crack half-length, c; and plate thickness t. Dimensions h and b remain fixed at five times the larger of a and c such that the K_I-values approximate those in a semi-infinite plate. The current work includes analyses of plates for a range of practical crack geometries of $a/c = 1/3$, $a/c = 1$ and $a/c = 2$ and crack depths of $a/t = 0.2$, $a/t = 0.5$ and $a/t = 0.8$. A specimen cross-section, illustrated in Fig. 8(b), indicates through-thickness material variation, assigned to follow the form $E(x) = E_1 e^{\beta x}$, where $E_1 = E(x=0)$, $E_2 = E(x=t)$, with β given by Eq. (1) such that $E_2/E_1 = 0.2$, 1.0 and 5.0. Poisson's ratio remains constant at 0.25 in all cases. Fig. 8(b) also illustrates the applied tensile stress, σ_t, and bending stress, σ_b, where $\sigma_b = 3M/bt^2$. Table 3 summarizes the surface-crack geometries, material properties, and temperature variations employed in this study.

Thermal loading conditions follow those used by Erdogan and Wu (1996) who analyzed a zirconia/Rene-41 composite with the properties listed in Table 4. Young's modulus (E), CTE (α), and conductivity (k)

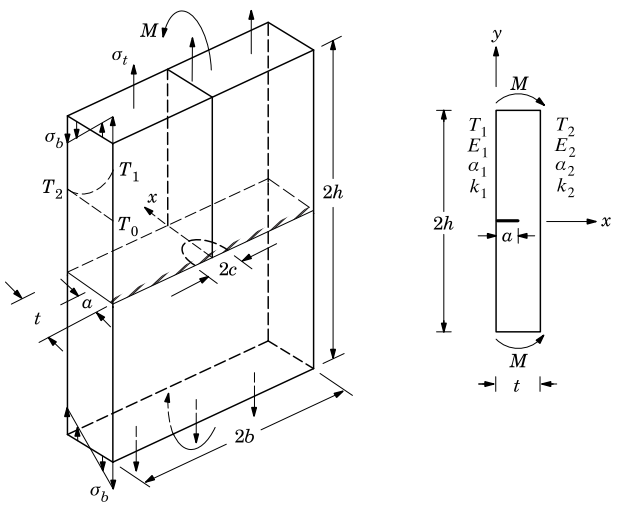

Fig. 8. (a) Surface crack specimen showing axial, bending and thermal loads. The hatched area illustrates the potential region for the "boundary layer" (see Section 6.3). Symmetry permits analysis using one quarter of the model. (b) Cross-section of plate showing unidirectional material variation from cracked face to uncracked face. Bending stress is calculated from total moment M as $\sigma_b = 3M/bt^2$.

Table 3
Specified surface-crack geometries, material properties, and temperature loads

Quantity	Specified values
a/c	1/3, 1, 2
a/t	0.2, 0.5, 0.8
E_2/E_1	0.2, 1.0, 5.0
v_2/v_1	1.0
T_1/T_2	5, 10, 20

Table 4
Properties for thermal loading of surface-crack specimens (Erdogan and Wu, 1996)

Material	E (GPa)	v	α (K^{-1})	k (Cal/mm sec K)
$(x = 0)$ Zirconia	151	0.33	1.0×10^{-5}	0.05
$(x = t)$ Rene-4l	219.7	0.33	1.67×10^{-5}	0.61

vary exponentially according to $E(x) = E_1 e^{\beta x}$, $\alpha(x) = \alpha_1 e^{\omega x}$, and $k(x) = k_1 e^{\eta x}$, where $(\cdot)_1$ is the property value at $x = 0$. The coefficients of nonhomogeneity, β, ω and η have values given by Eqs. (1) and (4). These material properties are taken as temperature independent.

Fig. 8(a) shows the qualitative temperature distribution which follows solution of the 1-D diffusion equation described in Section 2. The selected range of boundary temperatures includes: $T_1 = 5T_2$, $T_1 = 10T_2$ and $T_1 = 20T_2$, where $T_1 = T(x = 0)$ and $T_2 = T(x = t) = T_0$. To illustrate the application of Eq. (36) to thermal loading, the present work includes analyses of plates with the three crack geometries listed in Table 3, each with a crack depth of $a/t = 0.2$.

6.2. Conversion of J to normalized stress-intensity factor, K_{In}, for surface cracks

This paper reports values of the domain integral, Eq. (36), calculated at the corner nodes of all crack-front elements. Parametric angle, ϕ, measured in radians, describes the location of crack-front nodes on the crack-front for possible ranges of the ratio a/c (see Fig. 9). At each crack-front location ϕ, Eq. (39) yields K_I-values from J and $E_{(S)}$, the value of Young's modulus at that location. For through-thickness material variation and semi-elliptical cracks, $E_{(S)}$ at ϕ equals $E(x)$ at distance $x = a\sin\phi$ from the cracked surface.

A general form for mode-I stress-intensity factors for semi-elliptical surface cracks is

$$K_I = S\sqrt{\frac{\pi a}{Q}}F\left(\frac{a}{t},\frac{a}{c},\phi,P\right), \tag{42}$$

where $S = \sigma_t$ for tension, and $S = \sigma_b$ for bending. For plane-strain thermal loading, $S = \alpha_1 E_1 T_0/(1-\nu)$, and for plane-stress, $S = \alpha_1 E_1 T_0$ (Erdogan and Wu, 1996). Fig. 1 defines α_1, E_1, and T_0. The shape factor, Q, denotes the square of the complete elliptic integral of the second kind. $\sqrt{Q}$ equals half the arc length of an ellipse divided by the length of the major axis (Merkle, 1973), a ratio commonly approximated by

$$Q = \begin{cases} 1 + 1.464\left(\frac{a}{c}\right)^{1.65} & \text{for } a/c \leqslant 1, \\ 1 + 1.464\left(\frac{c}{a}\right)^{1.65} & \text{for } a/c > 1. \end{cases} \tag{43}$$

Function F in Eq. (42) includes the effects of plate dimensions, crack geometry, location along the crack-front and material property variation, represented by P. A normalized stress-intensity factor expressed by

$$K_{In} = \frac{K_I}{S\sqrt{\frac{\pi a}{Q}}} = F\left(\frac{a}{t},\frac{a}{c},\phi,P\right), \tag{44}$$

represents a "shape factor" for the geometry, material and loading conditions under consideration.

6.3. Stress-intensity factors at the intersection of the crack-front with the free surface

Researchers employ analytical and numerical techniques to examine the change in the singular behavior at the intersection of a 3-D crack-front with a traction-free surface (Hartranft and Sih, 1970; Benthem, 1977; Bazant and Estenssoro, 1979; Pook, 1994). These studies demonstrate the existence of a "boundary layer" very near the free surface over which a generalized stress-intensity factor may vary sharply. The change in singular behavior depends upon Poisson's ratio and the angle of intersection between the crack-front and the free surface, illustrated by ψ in Fig. 9(b). For FGMs, the length scale of material gradation

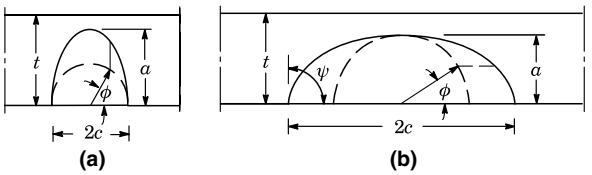

Fig. 9. Plan view of the crack plane shown in Fig. 8(a). (a) Measurement in radians of parametric angle, ϕ, for $a/c > 1.0$. (b) Parametric angle, ϕ, for $a/c \leqslant 1.0$, and intersection angle, ψ, describing the angle between the crack-front and free surface. For all models in this study, $\psi = 90°$.

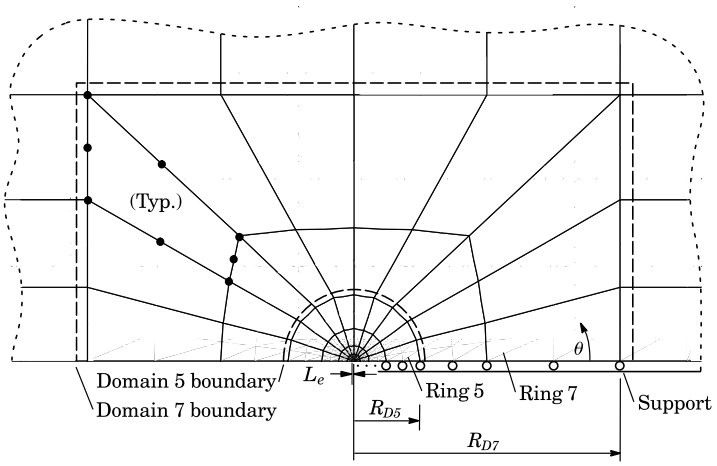

Fig. 10. Crack-front mesh with 7 rings of elements in the radial direction, and 10 elements along the θ direction. The ratio of L_e to plate thickness t, $L_e/t = 7.66 \times 10^{-4}$, describes the level of mesh refinement. R_D provides a measure of domain size.

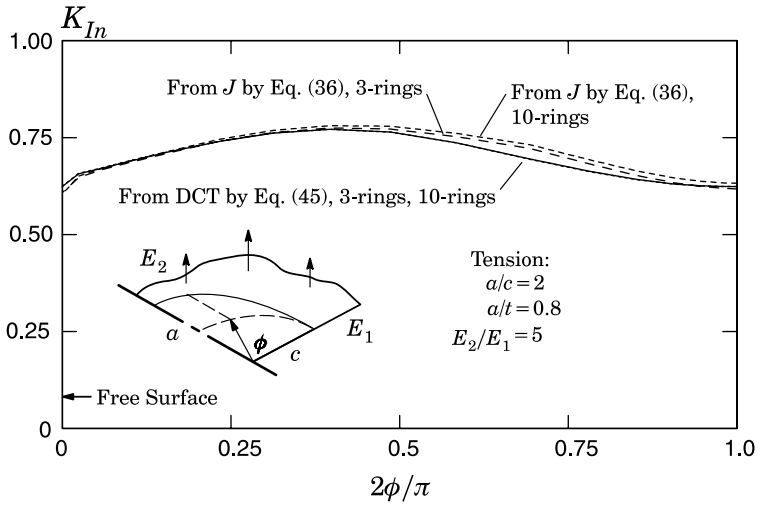

Fig. 11. Comparison of normalized stress-intensity factors, K_{In}, obtained using Eqs. (36) and (45) for 3-ring and 10-ring crack-front mesh refinements where $a/c = 2$ and $a/t = 0.8$.

(e.g. parameter $1/\beta$, where Eq. (1) defines β) should also affect the stress state and the size of the boundary layer. For a crack front that intersects the free surface at $\psi = 90°$, when Poisson's ratio is greater than zero, the stress singularity ($r^{-\lambda}$) in the boundary layer becomes weaker ($\lambda < 1/2$), and the mode-I stress-intensity factor tends toward zero at the surface (Pook, 1994).

Raju and Newman (1979) verify the decrease in stress-intensity factors near the free surface through a detailed mesh-refinement study of a semi-circular surface crack. More importantly, their study shows that the effects of the boundary layer are highly localized, and do not influence stress-intensity factors on the

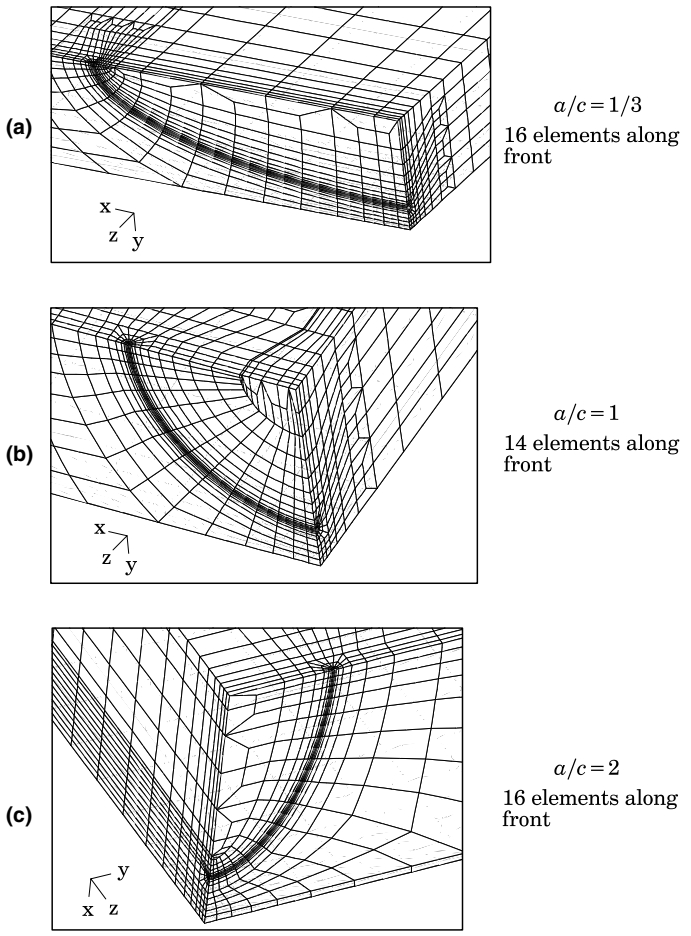

Fig. 12. Typical discretization along front for surface-crack configurations.

interior of the specimen. Chuntu and Yingzhi (1987), Li et al. (1998), Rajaram et al. (2000), Ayhan and Nied (2002) and Frangi (2002) also demonstrate the localized influence of the boundary layer on stress-intensity factors through numerical analyses of straight cracks and semi-circular, quarter-circular and semi-elliptical surface cracks. Nakamura and Parks (1988) estimate the region of influence of the corner singularity in semi-elliptical surface cracks as $\approx 0.03 \times a^2/c$, where a and c are the crack dimensions shown in Fig. 8. Because a detailed study of the boundary-layer influence in FGMs is not the focus of this paper, the present work does not include sufficient mesh refinement in this region to determine adequately the layer's size, or to capture the true variation of stress-intensity factors within the boundary layer. To acknowledge the effect of the weak corner singularity, however, for mechanical loading, the plane-stress conversion applies here to J-values calculated at the free surface, i.e. $\phi = 0$, and the plane-strain conversion applies here for $\phi > 0$. Although stress-intensity factors near $\phi = 0$ should tend toward zero in order to conform with theory, the nonzero values reported here represent average stress-intensity factors near the free surface (Raju and Newman, 1979). For thermal loading, plane-stress K_{In}-values obtained using Eqs. (39) and (44), exceed plane-strain values by a factor of $[(1-\nu)/(1+\nu)]^{1/2}$. To avoid

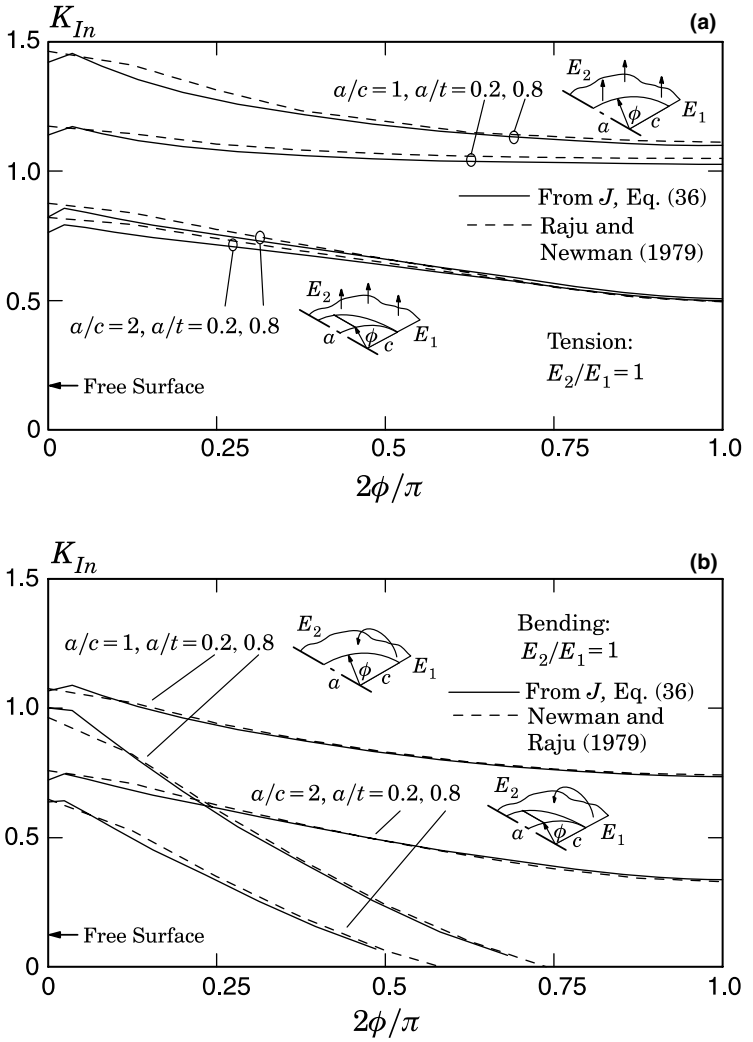

Fig. 13. Normalized K_I-values, K_{In}, for surface-cracked plates with homogeneous material having $a/c = 1$, 2, and $a/t = 0.2$, 0.8. Comparison of values generated using Eq. (36) with those of (a) Raju and Newman (1979) and (b) Newman and Raju (1979).

reporting an increase in K_{In}-values in the boundary layer, we simply omit stress-intensity factors at $\phi = 0$ for thermal loading.

6.4. Mesh refinement

A mesh that is adequately refined for the correct solution of a boundary-value problem of a homogeneous body may require further refinement in order to capture the effects of material gradients. To confirm adequate refinement of meshes used in this study, values of K_{In} published in the literature and those obtained here using the DCT verify values of K_{In} obtained from Eq. (36) for both homogeneous and non-homogeneous specimens.

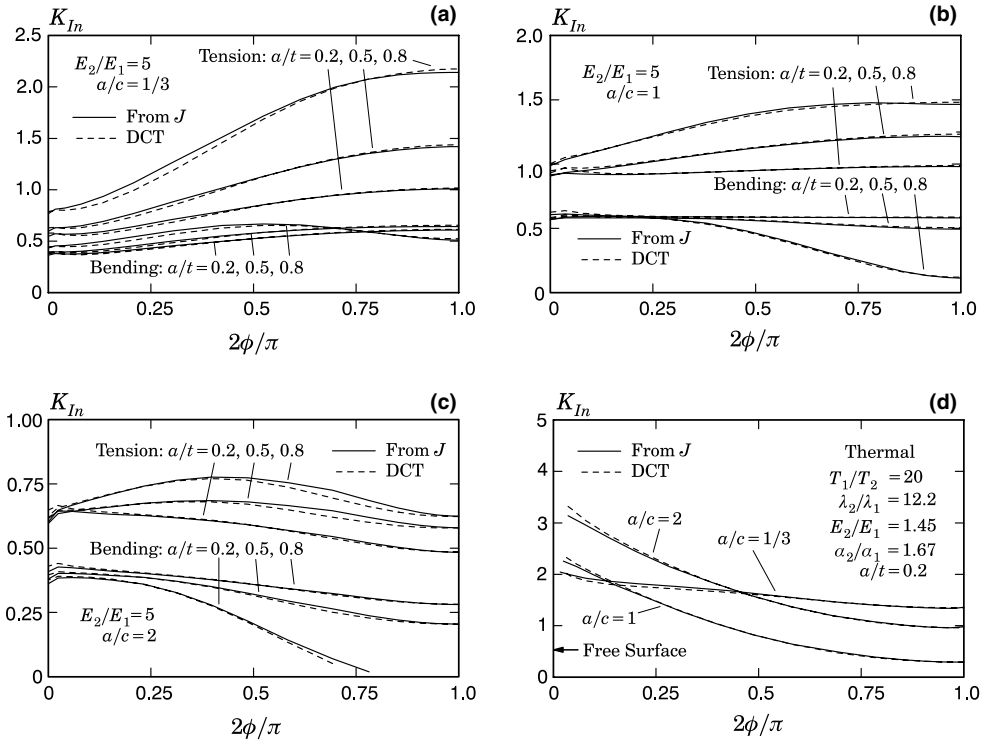

Fig. 14. (a) Comparison of normalized K_I-values from the J-integral, Eq. (36) and DCT, Eq. (45), for tension and bending with $E_2/E_1 = 5$, $a/t = 0.2$, 0.5, 0.8, and $a/c = 1/3$; (b) $a/c = 1$; (c) $a/c = 2$; (d) thermal loading with $T_1/T_2 = 20$, $a/t = 0.2$ and $a/c = 1/3$, 1, 2 (Material properties correspond to those for a zirconia/Rene-41 FGM. See Table 4).

For 2-D cracked configurations, Eischen (1987) and Jin and Noda (1994) prove that the near-tip displacement field for functionally graded materials has the same form as for homogeneous materials. Hartranft and Sih (1969) show that the singularity along a 3-D crack-front in homogeneous material (remote from boundaries) has the same form as the crack-tip singularity in a 2-D configuration. Based on these two results, the opening displacement of the crack-face, normal to the crack plane, has the asymptotic form

$$u_2 = \frac{4K_I}{E^*_{(S)}}\sqrt{\frac{r}{2\pi}}, \tag{45}$$

where u_2 denotes the displacement in the X_2-direction of the coordinate system shown in Fig. 3, K_I is the mode-I stress-intensity factor, and r is the distance behind and normal to the crack-front. The use of $E^*_{(S)}$ in Eq. (45) is justified by the equivalence of asymptotic crack-front fields in homogenous and functionally graded materials (Eischen, 1987; Jin and Noda, 1994).

The DCT utilizes the relationship between displacement and K_I expressed in Eq. (45) to estimate stress-intensity factors based on u_2 nodal displacements behind the crack front. Here, element boundaries on the crack-face define approximate normals to the crack front. Values of u_2 and r at several nodes along one boundary, when inserted into Eq. (45), permit the calculation of a K_I-value that corresponds to each node. A plot of these K_I-values vs. r yields an approximately linear relationship between K_I and r. The intersection

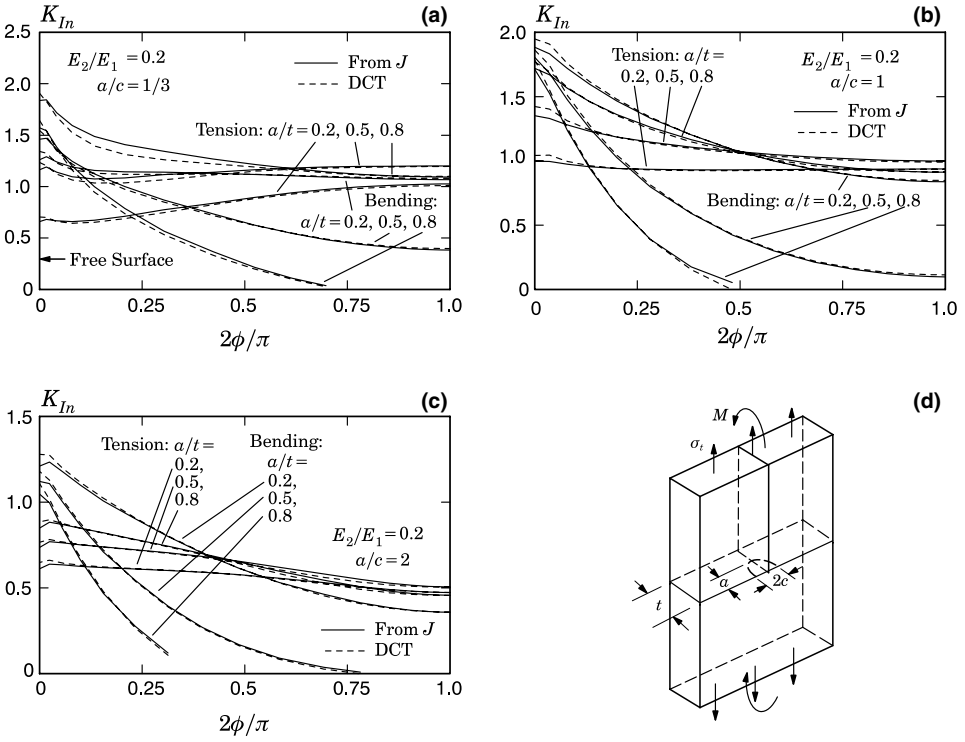

Fig. 15. (a) Comparison of normalized K_I-values from J, Eq. (36) and DCT, Eq. (45), for tension and bending with $E_2/E_1 = 0.2$, $a/t = 0.2$, 0.5, 0.8, and $a/c = 1/3$; (b) $a/c = 1$; (c) $a/c = 2$; (d) Specimen.

of this line with $r = 0$ provides the estimated crack-front K_I-value for the DCT. Eq. (44) describes the normalization of these values.

6.4.1. Effects of mesh refinement on K_I-values for FGM specimens

Stress-intensity factor solutions from four different meshes of a plate with crack geometry $a/t = 0.8$ and $a/c = 2$, and an exponential material variation where $E_2/E_1 = 5$, provide insight into the effects of mesh refinement on the values of K_{In}. Ten 20-noded, quarter-point, hexagonal elements with collapsed faces immediately surround each crack front in the θ direction (see Fig. 10). In the radial direction, the four meshes have respectively 3, 5, 7, and 10 rings of elements surrounding the crack-front, corresponding to the number of domains used to produce J-values. Sixteen elements lie along the crack-front between $\phi = 0$ and $\pi/2$. Fig. 10 shows a typical crack-front location in the local x_1–x_2 coordinate system for the 7-ring mesh. Ratios of crack-front element length, L_e, to plate thickness, t, L_e/t, range from 1.47×10^{-2} for the 3-ring mesh, to 5.41×10^{-5} for the 10-ring mesh. The 3-ring mesh has 7632 elements and 34 013 nodes, and the 10-ring mesh has 8752 elements and 39 053 nodes. The number of nodes and elements in each model reflects the large plate dimensions h and b. Increased mesh refinement in the four models focuses primarily on the crack-front region. Fig. 11 shows normalized K_I vs. location along the crack-front for $0 < \phi < \pi/2$, and compares K_{In} obtained through Eqs. (36) and (45) for the 3-ring and 10-ring models. The meshes yield results which show little variation between refinement levels, and which show close agreement between the two methods, i.e. Eqs. (36) and (45).

The reduced ($2 \times 2 \times 2$) integration triggers a small amount of hourglassing in crack-front elements for the 7-ring model, which becomes more pronounced in the 10-ring model. Hourglassing does not signifi-

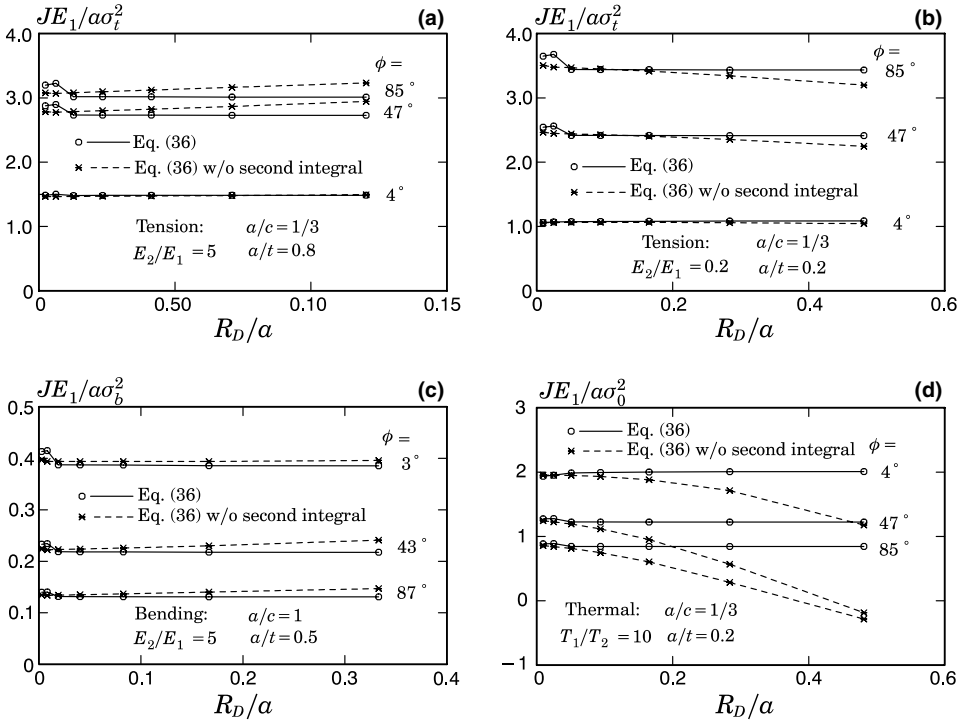

Fig. 16. Normalized J-values at three crack-front locations computed using Eq. (36) with and without the second integral. (a) Tension loading for $E_2/E_1 = 5$. (b) Tension loading for $E_2/E_1 = 0.2$. (c) Bending load, for $E_2/E_1 = 5$. (d) Thermal loading ($\sigma_0 = E_1\alpha_1 T_0/(1-\nu)$) for $T_1/T_2 = 10$ (see Fig. 8). Table 4 lists material properties.

cantly affect K_I in the 7-ring model—the refinement level selected to discretize all subsequent models of surface-cracked plates. Fig. 12 shows typical mesh refinement in the crack region for the three crack geometries analyzed in this study, i.e. $a/c = 1/3$, 1 and 2. J-values obtained from all 7-ring meshes are an average of domains three through seven.

6.4.2. Verification of K_I-values for homogeneous specimens

A comparison of K_I-values obtained from Eq. (36) with those reported by Newman and Raju (1979) verifies the present solution of the boundary-value problem for the homogeneous plate specimens. Fig. 13(a) compares values of K_{In} derived from Eq. (36) with the Raju and Newman (1979) solutions for tension loading of homogeneous material, crack geometries $a/c = 1$ and 2, and crack depths $a/t = 0.2$ and 0.8. Fig. 13(b) compares K_{In}-values from Eq. (36) with Newman and Raju (1979) solutions for the same models under bending. Bending loads cause portions of the crack-face to close. Without contact surfaces, finite-element solutions for these cases permit spurious crack-face displacements (i.e. crack-face interpenetration) which cause some domains to produce negative J-values. Newman and Raju (1979) list the negative values; here we report only positive values. Lee and Erdogan (1998) and Anifantis (2001) describe techniques to include crack-face contact in 2-D cases. Fig. 13 shows agreement between K_{In}-values obtained from Eq. (36) for both tension and bending loads with the Newman and Raju solutions.

6.4.3. Verification of K_I-values for functionally-graded specimens

For FGM cases, the good agreement between K_{In}-values obtained using Eq. (36) and those obtained using the DCT confirms that the adopted level of mesh refinement captures the effects of material property

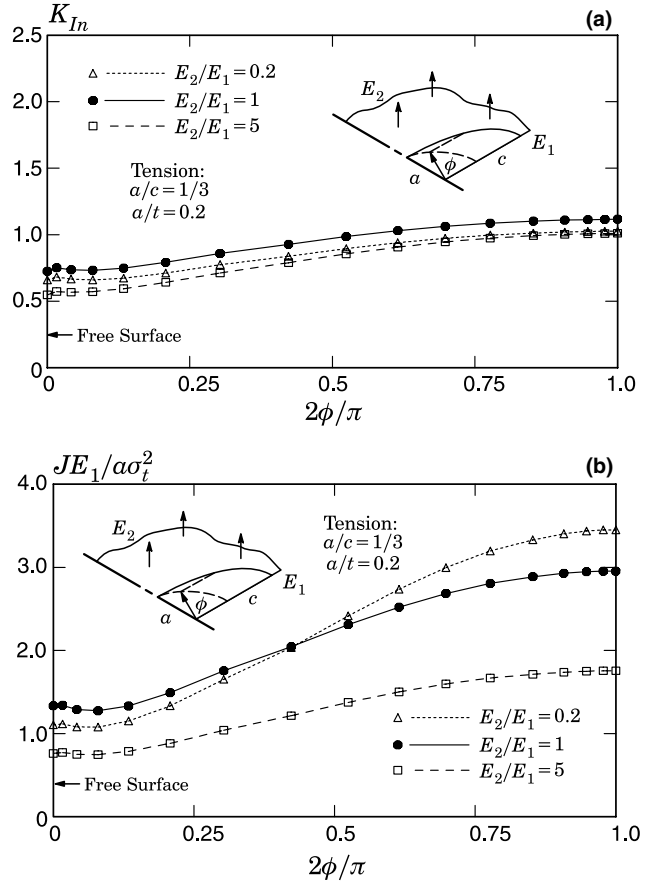

Fig. 17. (a) Normalized K_I-values along a front under remote tension loading for a crack with $a/c = 1/3$ and $a/t = 0.2$. (b) Normalized values of J along the crack-front corresponding to the K_{In}-values in (a).

gradients. Previous applications of the DCT to 2-D models for FGMs include Li et al. (1999), Marur and Tippur (2000), Rousseau and Tippur (2001) and Kim and Paulino (2002a). For an exponential material variation with $E_2/E_1 = 5$, Fig. 14(a)–(c) compares tension and bending results for each crack geometry and crack depth. Fig. 14(d) compares results for thermally-loaded plates with three crack geometries: $a/c = 1/3$, 1, and 2, each with crack depth $a/t = 0.2$. The specified surface temperature ratio is $T_1/T_2 = 20$, with the through-thickness temperature distribution as described in Section 2 (and shown schematically in Fig. 8).

K_{In}-values for all loading cases show good agreement between the two methods (i.e. from J and the DCT), with the largest difference occurring along crack-front sections with high curvature. In Fig. 14(a), the largest difference for $a/c = 1/3$ is less than 7% of the smaller value. For $a/c = 2$, the maximum difference in Fig. 14(c) is less than 5% of the smaller value. Fig. 15(a)–(c) compares K_{In}-values derived from Eq. (36) with K_{In}-values obtained via the DCT for all crack geometries and crack depths, for an exponential material variation with $E_2/E_1 = 0.2$. In this case, a maximum difference slightly greater than 7% occurs under tension loading near $\phi = 0.25$ for $a/c = 1/3$ and $a/t = 0.8$ (see Fig. 15(a)).

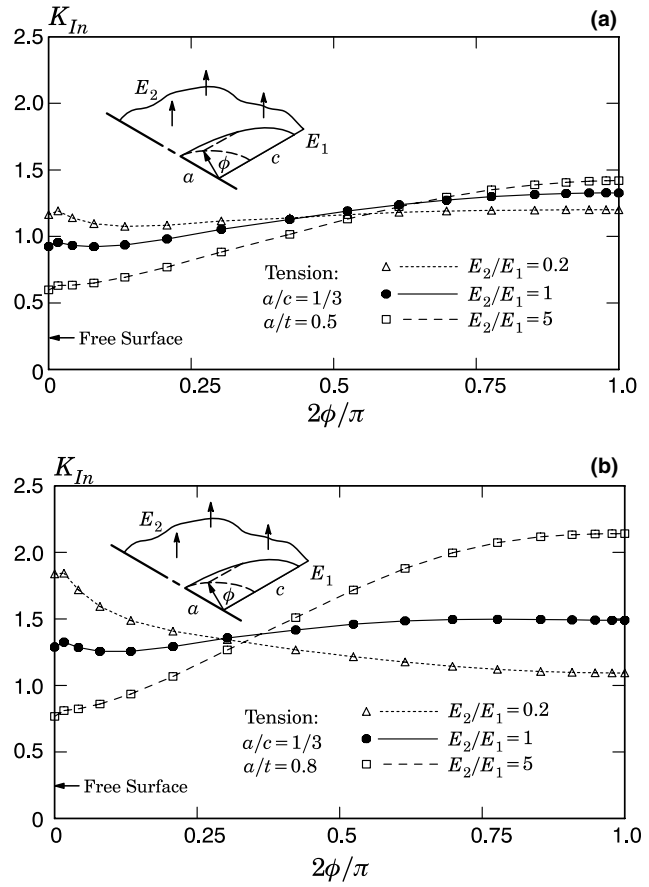

Fig. 18. Normalized K_I-values along a crack-front under remote tension loading for a crack with $a/c = 1/3$ and (a) $a/t = 0.5$; (b) $a/t = 0.8$.

6.5. Effect of material gradient terms on J-values

Fig. 16(a)–(d) shows J-values, calculated with and without the second integral of Eq. (36), at three locations, ϕ, along the crack front for four different combinations of crack geometry and loading. Each curve in the figure has seven points that correspond to the seven domains used to calculate J-values. Here, R_D/a equals the radius of the domain, measured at $\phi = \pi/2$, divided by the crack depth, a. Fig. 10 illustrates R_D, which is measured ahead of the crack-front on the plane of symmetry. For the purpose of interpreting the results shown in these figures, Eq. (28) is more intuitive than its equivalent used for numerical implementation, Eq. (36). For tension and bending loads, the contribution of gradient terms at small ϕ is insignificant for all domains. This reflects the vanishing of $E_{,1}(\boldsymbol{x})$ as the crack-front normal X_1, becomes orthogonal to the direction of material variation. Fig. 16(a) and (c) shows that for $E_2/E_1 = 5$, omission of gradient terms leads to increased J-values as the domain size increases. This increase arises from an increase in both $\partial W/\partial E(\boldsymbol{x})$ and $E_{,1}(\boldsymbol{x})$ in the direction of the crack-front normal. For a softening material, i.e. $E_2/E_1 = 0.2$, J-values decrease as the domain size increases (see Fig. 16(b)). For the thermally-loaded specimens, the second integrand of Eq. (36) shows a much greater influence on J than in the

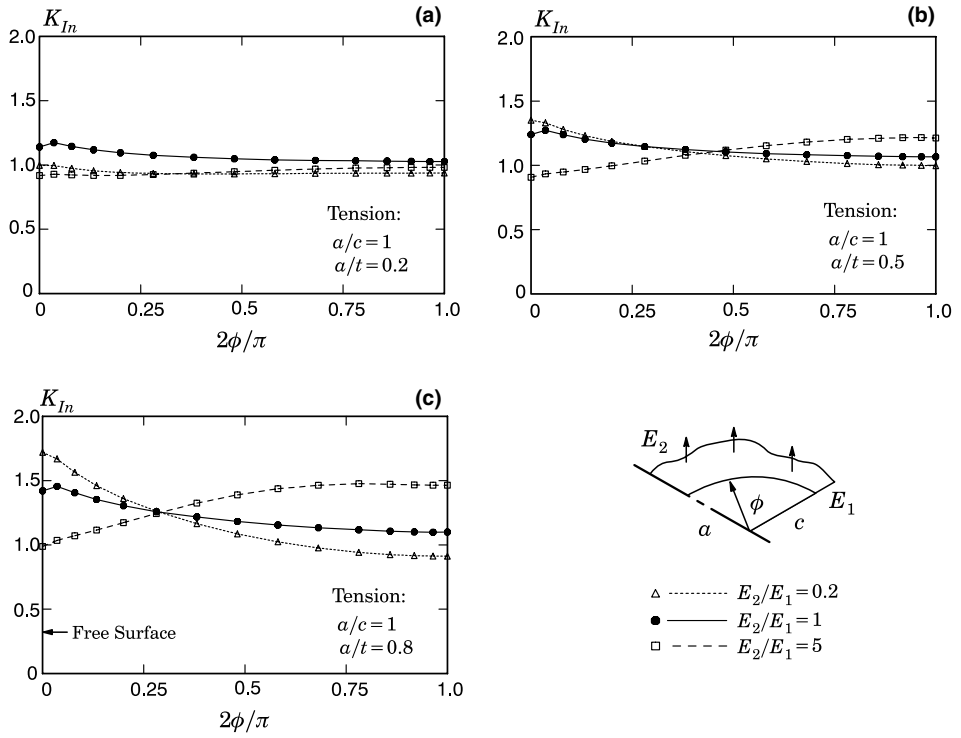

Fig. 19. (a) Normalized K_I-values along a crack-front loaded in remote tension, with $a/c = 1$, $E_2/E_1 = 0.2$, 5 and 1, and $a/t = 0.2$, (b) $a/t = 0.5$, and (c) $a/t = 0.8$.

tension and bending cases, as seen in Fig. 16(d). Referring to Eqs. (28) and (32), when $\phi = 0$, the gradient terms $E_{,1}(\boldsymbol{x})$, $\alpha_{,1}(\boldsymbol{x})$, and $\Theta_{,1}(\boldsymbol{x})$ all vanish. At other front locations, the gradient terms become significant as the domain size increases, reflecting the combined effects of thermal loading and material gradients on J.

For all loading cases, the relative contribution of the second integrand increases with domain size, and becomes necessary to maintain domain independence of the J-values. Because R_D/a ratios are small for the domains employed to generate the curves shown in Fig. 16, domain dependence of J-values is not as significant as that shown in Fig. 7(c) and (d) for an SE(T) specimen where R_D/a are larger. As domains decrease in size, the magnitude of the second integral of Eq. (36) becomes much smaller than the first (conventional) integral. This difference in relative magnitude is a function of the derivative ($q_{,1}$) in the first integral. Fig. 6 shows that q decreases from unity at the crack-front to zero at the outer boundary of the domain. As the domain shrinks in size, the distance from the crack-front to the outer boundary of the domain also shrinks, and causes the derivative of q to become very large, thereby heavily weighting the first integral (Gu et al., 1999). This trend in J with decreasing domain size agrees with observations made by Aoki et al. (1982), Tohgo et al. (1996) and Gu et al. (1999) who suggest that very small, near-tip domains yield accurate values of J in an FGM without including gradient terms—at least for linear-elastic analyses. This eliminates one advantage of the J-integral, however, which is good accuracy when evaluated over large domains in a relatively coarse mesh. Path independence, which does not generally result without the use of gradient terms, indicates an acceptable level of mesh refinement. The omission of gradient terms removes these two advantages of J-integral calculations.

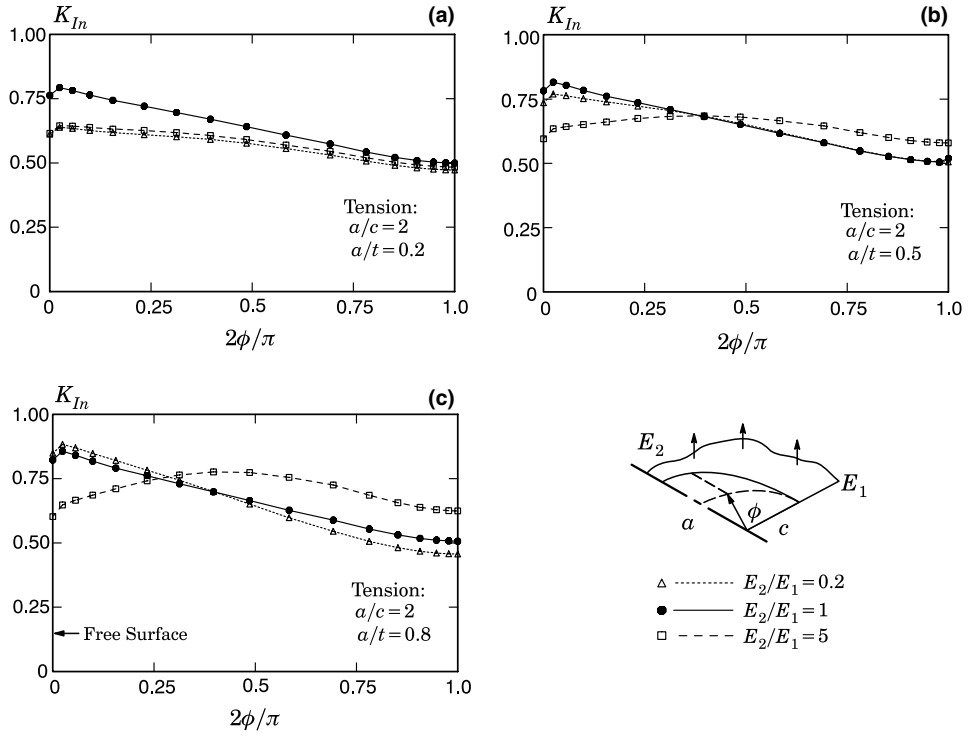

Fig. 20. (a) Normalized K_I-values along a crack-front loaded in remote tension, with $a/c = 2$, $E_2/E_1 = 0.2$, 5 and 1, and $a/t = 0.2$, (b) $a/t = 0.5$, and (c) $a/t = 0.8$.

7. Stress-intensity factors for surface cracks in FGM plates

7.1. Tension load

Figs. 17–20 show K_{In}-values for a selected range of specimen and crack geometries, all loaded by remote tension. Because the plane-stress assumption applies to the J–K_{In} conversion at the free surface, and the plane-strain assumption applies at interior points (see Eq. (39) and Section 6.3), each of the curves exhibits a small kink between values of K_{In} at $\phi = 0$ and the first interior point. To simplify discussions here, the term "soft" applies to specimens with a material variation of $E_2/E_1 = 0.2$, and "stiff" applies to specimens with a variation of $E_2/E_1 = 5.0$.

Fig. 17(a) shows that for $a/c = 1/3$ and $a/t = 0.2$, K_{In}-values at all points along the crack-front are greater in the homogeneous material than in the soft material, and greater in the soft material than in the stiff material. To explain this perhaps unexpected result, Fig. 17(b) shows the corresponding energy release rates (J-values). The energy release rate along the deeper portion of the crack is higher in the soft material than in the homogeneous material, as expected. In this figure, the values of J for $E_2/E_1 = 5.0$ clearly show that as Young's modulus increases along the crack-front, the energy release rate decreases with respect to the homogeneous material. As the modulus decreases along the crack-front, the energy release rate increases with respect to the homogeneous material, as demonstrated by the J-values for $E_2/E_1 = 0.2$. Because of the proximity of the J-curves for the soft and homogeneous materials, the values of $E_{(S)}$ used to convert J into K_{In} drive the stress-intensity factors of the soft material below the stress-intensity factors of the homogeneous material.

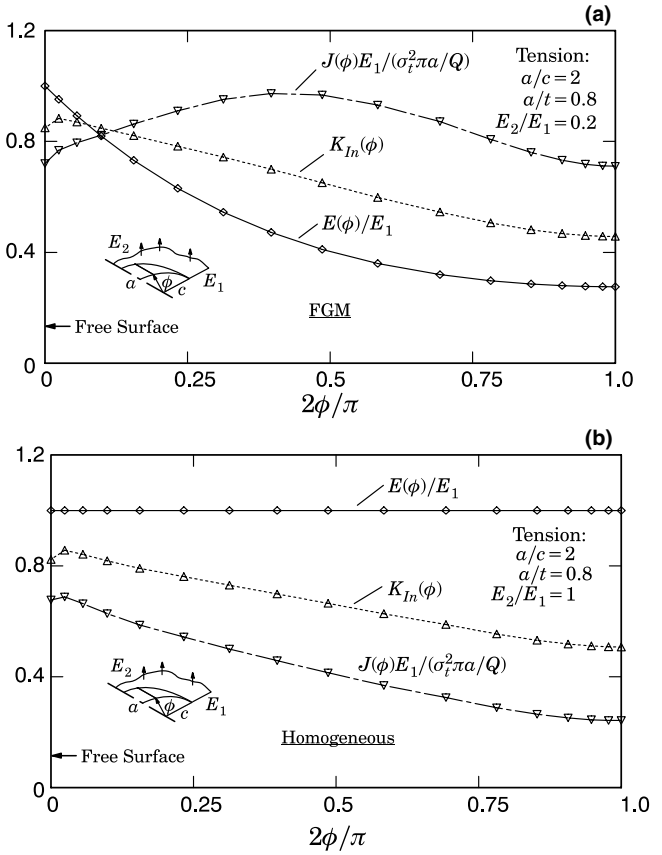

Fig. 21. Comparison of trends in J, K_{In} and E along a crack front under tensile loading for the geometry $a/c = 2$ and $a/t = 0.8$, in material where (a) $E_2/E_1 = 0.2$ and (b) $E_2/E_1 = 1$. In FGMs, the location, ϕ, of maximum J along the curved crack-front does not necessarily correspond to the location of maximum K_{In}.

For each ratio of a/c, an increase in crack depth in the soft material causes the magnitude of K_{In} near the cracked surface to increase relative to the value of K_{In} at the deepest point along the crack. For all ratios of a/c, an increase in crack depth in the stiff material causes the magnitude of K_{In} to increase overall, but causes K_{In} near the cracked surface to decrease relative to the value of K_{In} at the deepest point along the crack. In all materials, for a constant ratio of a/t, a decrease in a/c causes the value of K_{In} near the cracked surface to increase relative to the value of K_{In} at the deepest point in the crack.

In all geometries of nonhomogeneous material examined here, Young's modulus, $E_{(S)}$, varies along the curved crack front. Because $E_{(S)}$ influences the conversion from J to K_I (see Eq. (39)), the crack-front location, ϕ, of maximum J does not necessarily correspond to the location of maximum K_I. The curves in Fig. 21(a) show trends in the variation of J, K_{In} and E along the front of a surface crack under remote tension loading with $a/c = 2$, $a/t = 0.8$ and $E_2/E_1 = 5$. Here $J_n(\phi) = J(\phi)E_1/(\sigma_t^2\pi a/Q)$ defines a normalized value of J along the crack-front, and $E_n(\phi) = E(\phi)/E_1$ defines a normalized value of Young's modulus. In this figure, the maximum J-value occurs near $2\phi/\pi \approx 0.5$, while the maximum K_{In} occurs near the free surface. Fig. 21(b) shows trends in J, K_{In} and E for an identical crack in a homogeneous material. In this case, the crack-front locations of maximum–minimum J correspond to locations of maximum–minimum K_I.

Table 5
Normalized stress-intensity factors, K_{In}, along the crack-front for specimens loaded in tension

a/c	$2\phi/\pi$	Tension								
		$a/t = 0.2$			$a/t = 0.5$			$a/t = 0.8$		
		E_2/E_1			E_2/E_1			E_2/E_1		
		0.2	1.0	5.0	0.2	1.0	5.0	0.2	1.0	5.0
1/3	0.000	0.660	0.725	0.548	1.164	0.925	0.598	1.838	1.289	0.767
	0.125	0.669	0.744	0.589	1.076	0.932	0.685	1.502	1.255	0.922
	0.250	0.739	0.822	0.673	1.098	1.013	0.819	1.378	1.321	1.155
	0.375	0.813	0.901	0.760	1.131	1.100	0.964	1.298	1.395	1.413
	0.500	0.882	0.972	0.840	1.158	1.176	1.104	1.228	1.452	1.670
	0.625	0.944	1.035	0.912	1.183	1.243	1.233	1.172	1.487	1.896
	0.750	0.990	1.080	0.966	1.195	1.291	1.334	1.128	1.498	2.052
	0.875	1.016	1.106	0.997	1.199	1.319	1.396	1.102	1.495	2.126
	1.000	1.027	1.117	1.011	1.200	1.327	1.420	1.094	1.490	2.141
1	0.000	0.997	1.140	0.917	1.351	1.240	0.907	1.720	1.421	0.988
	0.125	0.957	1.122	0.919	1.238	1.209	0.965	1.475	1.361	1.109
	0.250	0.936	1.082	0.923	1.161	1.155	1.019	1.297	1.275	1.217
	0.375	0.930	1.061	0.936	1.109	1.124	1.075	1.171	1.220	1.320
	0.500	0.931	1.046	0.950	1.071	1.101	1.125	1.073	1.176	1.400
	0.625	0.933	1.038	0.963	1.041	1.087	1.166	1.001	1.145	1.451
	0.750	0.935	1.034	0.974	1.019	1.078	1.197	0.951	1.123	1.475
	0.875	0.936	1.029	0.979	1.004	1.070	1.212	0.922	1.105	1.470
	1.000	0.938	1.027	0.981	0.997	1.067	1.213	0.912	1.100	1.465
2	0.000	0.612	0.763	0.615	0.736	0.782	0.596	0.849	0.823	0.602
	0.125	0.623	0.755	0.636	0.746	0.774	0.656	0.836	0.806	0.698
	0.250	0.608	0.716	0.625	0.719	0.731	0.677	0.775	0.755	0.748
	0.375	0.595	0.677	0.610	0.690	0.689	0.685	0.712	0.707	0.774
	0.500	0.574	0.637	0.588	0.651	0.646	0.679	0.643	0.659	0.772
	0.625	0.547	0.595	0.561	0.606	0.603	0.659	0.577	0.612	0.746
	0.750	0.516	0.554	0.529	0.561	0.560	0.629	0.519	0.566	0.700
	0.875	0.486	0.516	0.499	0.522	0.521	0.595	0.475	0.525	0.648
	1.000	0.473	0.499	0.484	0.506	0.504	0.580	0.457	0.507	0.625

To tabulate these normalized stress-intensity factors, cubic-spline interpolation provides estimates of K_{In} at equally spaced (ϕ) crack-front locations in the range $0 \leqslant \phi \leqslant \pi/2$. Table 5 lists normalized K_I-values for the selected surface crack/material combinations under remote tension loading. Because the calculation of J occurs at a larger number of crack-front locations than the tabulated data reflects, the tables do not necessarily capture the exact maximum–minimum values of K_{In}. For example, Fig. 20(c) shows a maximum value of $K_{In} = 0.857$ at $\phi = 0.024$ for $E_2/E_1 = 1$, whereas Table 5 lists a maximum value of $K_{In} = 0.823$ at $\phi = 0.0$.

7.2. Bending load

Figs. 22–24 show K_{In}-values for selected crack geometries under remote through-bending load. For some crack geometries, bending causes crack-face nodes to penetrate the crack plane, thereby producing negative stress-intensity factors. Figures and tables for specimens under bending omit the unrealistic negative values.

Figs. 22–24 show that an increase in crack depth causes stress-intensity factors at the deepest part of the crack to decrease, which reflects the decreased stress from bending. As expected, the decrease in K_{In} is most

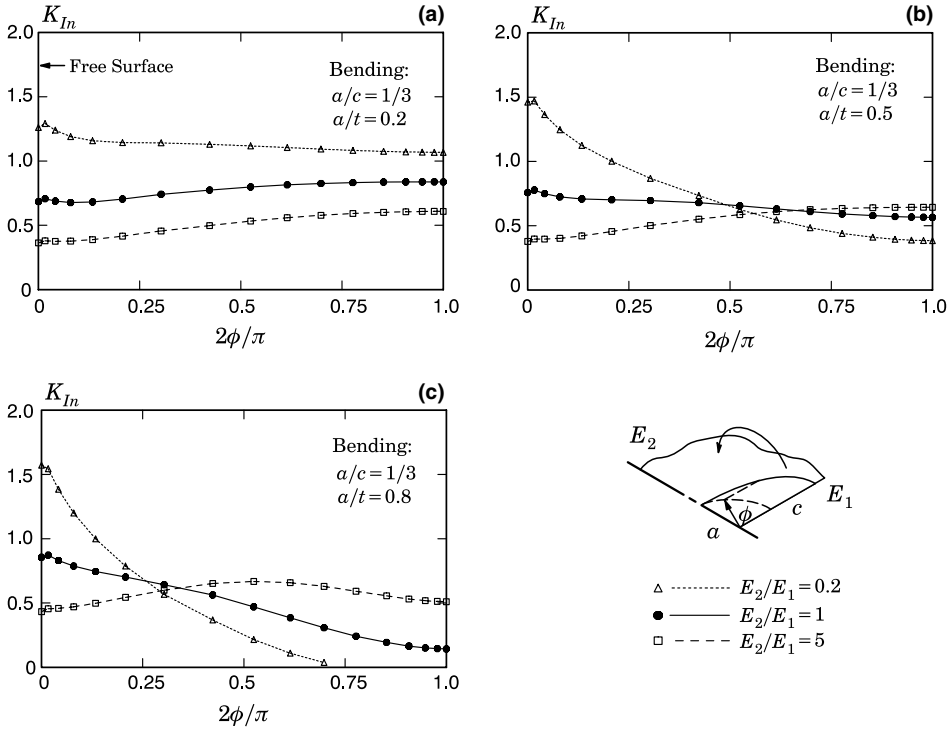

Fig. 22. (a) Normalized K_I-values along a crack-front loaded in remote bending, with $a/c = 1/3$, $E_2/E_1 = 0.2$, 5 and 1, and $a/t = 0.2$, (b) $a/t = 0.5$, and (c) $a/t = 0.8$.

pronounced in the soft material, and smallest in the stiff material. For crack geometry $a/c = 1/3$ (Fig. 22), the stress-intensity factor near the cracked surface increases slightly as crack depth increases. The increase is largest in the soft material, and smallest in the stiff material. When $a/c = 1$ (Fig. 23) and $a/c = 2$ (Fig. 24), the stress-intensity factor near the cracked surface decreases slightly with crack depth. The decrease is again largest in the soft material, and smallest in the stiff material.

In Figs. 22–24, for a constant value of a/t, the variation in stress-intensity factor near the cracked surface is not monotonic with increasing a/c, whereas K_{In} at the deepest point of the crack decreases monotonically with increasing a/c. Near the cracked surface, the stress intensity increases when the crack geometry changes from $a/c = 1/3$ to 1 (from Figs. 22, 23), but decreases when the geometry changes from $a/c = 1$ to 2 (from Figs. 23, 24). At the deepest point of the crack, the value of K_{In} decreases for each increase in crack depth, i.e. from $a/c = 1/3$ to 1 to 2 (Figs. 22–24). When $a/c = 1/3$ and $a/t = 0.8$, Fig. 22(c), the stress-intensity factor reaches its maximum value at a point along the crack-front between the cracked surface and the deepest point on the crack front.

Table 6 lists normalized K_I-values for the selected surface crack/material combinations under bending load. Dashes in the table replace otherwise negative stress-intensity factors. Cubic-spline interpolation again yields estimates of K_{In} at evenly-spaced (ϕ) crack-front locations in the range $0 \leqslant \phi \leqslant \pi/2$.

7.3. Thermal loading

The material properties and thermal boundary conditions for analyses performed here follow those used by Erdogan and Wu (1996) as described in Section 2. At crack-front locations interior to the specimen,

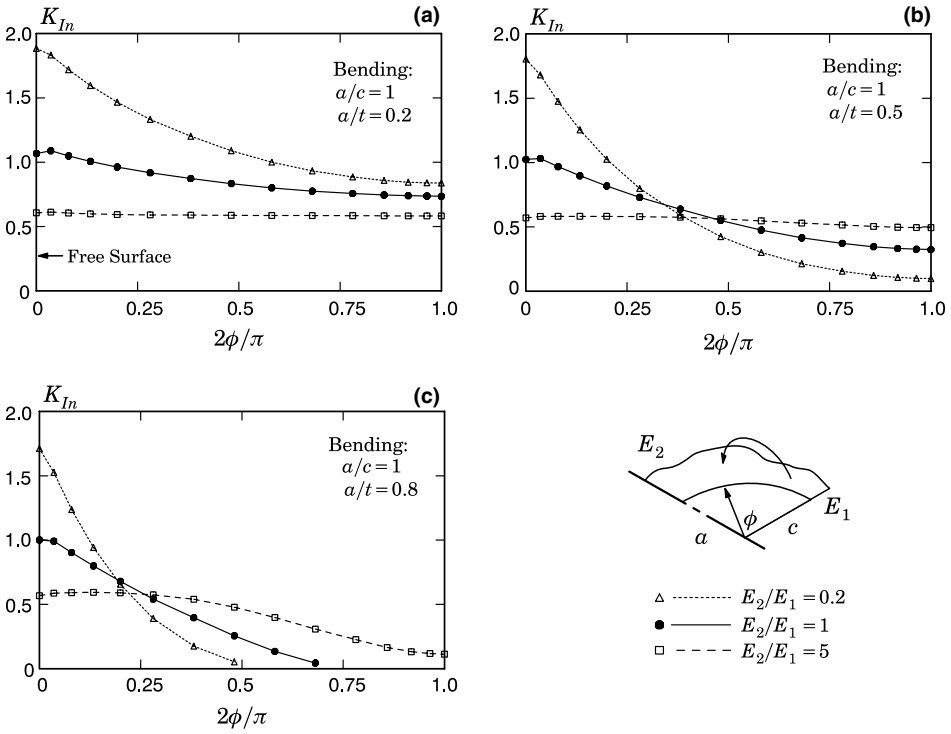

Fig. 23. (a) Normalized K_I-values along a crack-front loaded in remote bending, with $a/c = 1$, $E_2/E_1 = 0.2$, 5 and 1, and $a/t = 0.2$, (b) $a/t = 0.5$, and (c) $a/t = 0.8$.

Eqs. (39) and (41) here produce normalized K_I-values using the plane strain conversion. We omit stress-intensity factors at the free surface ($\phi = 0$) (see discussion in Section 6.3).

Fig. 25(a)–(c) shows normalized stress-intensity factors, K_{In}, for surface cracks under thermal loading, where the crack geometry includes three ratios of a/c, and a fixed crack depth of $a/t = 0.2$. Table 4 lists the material properties, and Fig. 8 illustrates the thermal gradient where the temperature at the cracked surface, T_1, equals 5, 10 and 20 times the temperature at the uncracked face, T_2. As the ratio of crack depth to crack length, a/c, becomes larger, the variation in stress-intensity factor drops more steeply from a maximum near $\phi = 0$ to a minimum at $2\phi/\pi = 1$. As a/c increases from 1/3 to 1 to 2, the magnitude of K_{In} at the deepest point of the crack, $2\phi/\pi = 1$, decreases monotonically. The value of K_{In} near the cracked surface increases as a/c grows from 1/3 to 1, and then decreases as a/c grows from 1 to 2. Table 7 lists normalized K_I-values for the selected surface crack/material combinations under thermal loads.

8. Summary and conclusions

This paper describes a domain integral formulation suitable to compute J-integral values along 3-D crack fronts in fracture specimens and components constructed of isotropic, functionally graded materials (FGMs). Within a finite element setting, material property values are specified at the model nodes with standard isoparametric interpolations to define integration point values. This approach coupled with the

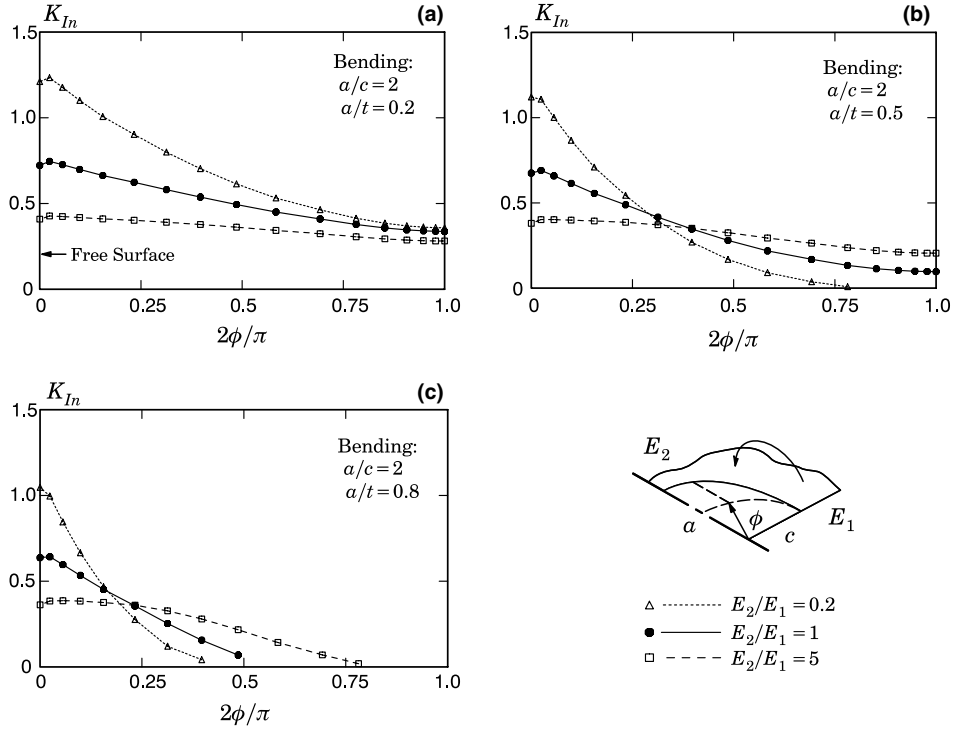

Fig. 24. (a) Normalized K_I-values along a crack-front under remote bending, with $a/c = 2$, $E_2/E_1 = 0.2$, 5 and 1, and $a/t = 0.2$, (b) $a/t = 0.5$, and (c) $a/t = 0.8$.

proposed domain integral thus accommodates effectively arbitrary, smooth gradations of material properties. The proposed numerical procedures to evaluate the domain integral use conventional quantities generated in a finite element solution and may thus be implemented in a post-processor. The present study explores the numerical implementation with applications to mode-I configurations in 2-D and 3-D having linear-elastic response and subjected to thermomechanical loading. For simple 2-D configurations, the available analytical solutions for an edge crack loaded remotely by tension and by temperature gradients support verification of stress-intensity factors derived from J-values computed with the proposed domain integral. In 3-D surface crack configurations, the displacement correlation technique yields pointwise values of stress-intensity factors along crack fronts for verification of corresponding factors computed with the domain integral procedure. The discussions also address mesh refinement levels required to resolve the solution gradients ahead of the crack-front in FGMs, to obtain path independence of the J-values, and to evaluate various contributions of the domain integral. These results demonstrate the utility and accuracy of using the proposed domain integral to derive 2-D and 3-D stress-intensity factors for FGMs.

A parametric study provides stress-intensity factors along crack fronts derived using the proposed domain integral for plates containing semi-elliptical surface cracks. This initial set of 3-D stress-intensity factors covers a practical range of crack sizes, aspect ratios and gradations of isotropic material properties (elastic modulus and coefficient of thermal expansion). Loadings considered include remote tension, bending and through-thickness temperature gradients. All configurations reflect mode-I conditions

Table 6
Normalized stress-intensity factors, K_{In}, along the crack front for bending loads

a/c	$2\phi/\pi$	Bending								
		$a/t = 0.2$			$a/t = 0.5$			$a/t = 0.8$		
		E_2/E_1			E_2/E_1			E_2/E_1		
		0.2	1.0	5.0	0.2	1.0	5.0	0.2	1.0	5.0
1/3	0.000	1.261	0.684	0.364	1.461	0.758	0.377	1.572	0.856	0.433
	0.125	1.160	0.680	0.387	1.141	0.710	0.417	1.028	0.752	0.494
	0.250	1.141	0.721	0.434	0.939	0.699	0.476	0.682	0.676	0.570
	0.375	1.136	0.762	0.482	0.787	0.687	0.533	0.442	0.597	0.635
	0.500	1.121	0.793	0.525	0.651	0.661	0.579	0.250	0.494	0.667
	0.625	1.104	0.816	0.562	0.537	0.629	0.612	0.098	0.375	0.656
	0.750	1.086	0.830	0.588	0.453	0.597	0.632	–	0.263	0.605
	0.875	1.073	0.837	0.603	0.403	0.576	0.641	–	0.181	0.546
	1.000	1.068	0.838	0.608	0.384	0.565	0.643	–	0.143	0.510
1	0.000	1.884	1.067	0.607	1.805	1.025	0.570	1.712	1.001	0.568
	0.125	1.614	1.012	0.599	1.286	0.908	0.582	0.984	0.815	0.594
	0.250	1.380	0.934	0.591	0.878	0.762	0.581	0.480	0.592	0.581
	0.375	1.210	0.876	0.589	0.603	0.643	0.576	0.187	0.405	0.543
	0.500	1.070	0.827	0.587	0.398	0.535	0.560	0.054	0.232	0.465
	0.625	0.968	0.788	0.586	0.259	0.447	0.539	–	0.087	0.359
	0.750	0.899	0.762	0.585	0.171	0.385	0.520	–	–	0.251
	0.875	0.853	0.743	0.583	0.117	0.341	0.502	–	–	0.155
	1.000	0.838	0.735	0.582	0.098	0.324	0.494	–	–	0.113
2	0.000	1.211	0.723	0.409	1.121	0.675	0.380	1.047	0.637	0.362
	0.125	1.057	0.683	0.415	0.792	0.587	0.397	0.569	0.496	0.381
	0.250	0.881	0.615	0.400	0.511	0.474	0.384	0.240	0.334	0.354
	0.375	0.727	0.548	0.381	0.298	0.364	0.357	0.049	0.180	0.293
	0.500	0.601	0.487	0.359	0.156	0.270	0.321	–	0.060	0.206
	0.625	0.504	0.434	0.336	0.068	0.198	0.283	–	–	0.115
	0.750	0.430	0.389	0.312	0.015	0.145	0.247	–	–	0.030
	0.875	0.378	0.352	0.291	–	0.109	0.217	–	–	–
	1.000	0.358	0.337	0.281	–	0.097	0.205	–	–	–

Dashes replace negative stress-intensity factors caused by interpenetration of crack faces.

(geometry, boundary conditions and loadings) with material properties that vary only in the thickness direction. The computed stress-intensity factors are presented in a standard nondimensional form for surface cracks using both graphical and tabular formats. The presence of the material property gradations introduces some unusual trends in K_I-values along the crack fronts (compared to those for surface cracks in homogenous materials as characterized by the Newman–Raju solutions). Moreover, unlike configurations with homogenous material properties, the locations of maximum J and maximum K_I do not necessarily coincide in the presence of material property gradations. The present set of 3-D solutions, while not exhaustive, does provide insights into the expected complexities of surface crack behavior in FGMs.

Our ongoing work considers applications of the proposed domain integral to compute J-values in surface cracks for metal-ceramic FGMs that undergo elastic–plastic deformations. The preliminary results again show good path independence of the J-values. Such J-values may prove useful to characterize the intensity of elastic–plastic crack-front fields in FGM specimens.

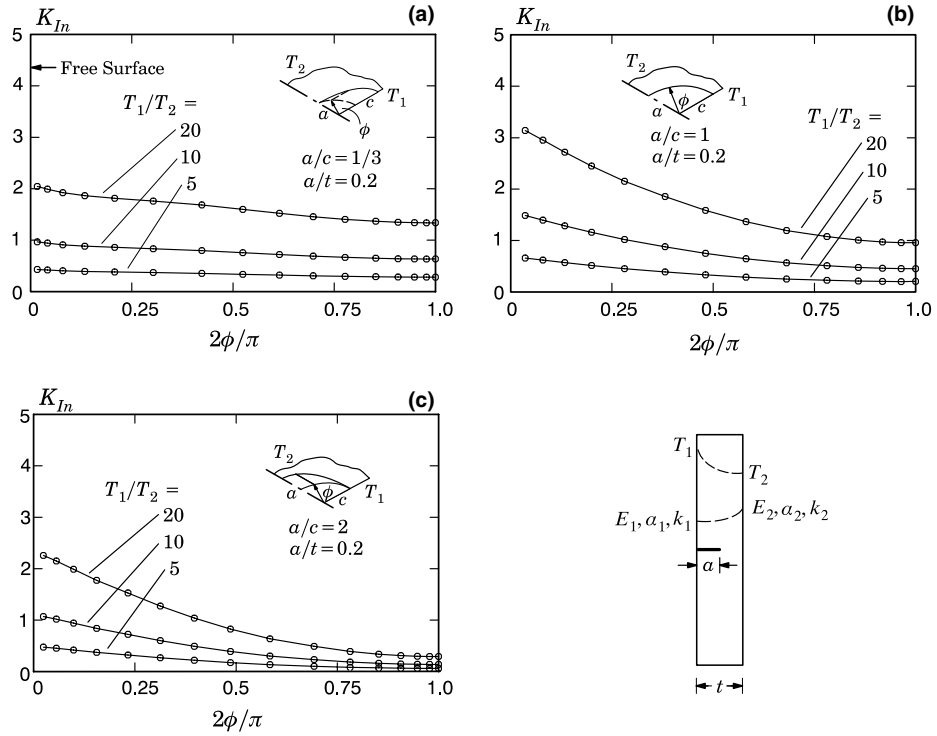

Fig. 25. Normalized K_I-values for a specimen under thermal loading with $a/t = 0.2$, $T_1/T_2 = 5$, 10 and 20, and (a) $a/c = 1/3$, (b) $a/c = 1$, and (c) $a/c = 2$. Material properties are listed in Table 4.

Table 7
Normalized stress-intensity factors, K_{In}, along the crack front for thermal loading

a/t	$2\phi/\pi$	Thermal loading								
		$a/c = 1/3$			$a/c = 1$			$a/c = 2$		
		T_1/T_2			T_1/T_2			T_1/T_2		
		5	10	20	5	10	20	5	10	20
0.2	0.000	–	–	–	–	–	–	–	–	–
	0.125	0.393	0.884	1.866	0.582	1.309	2.765	0.395	0.888	1.874
	0.250	0.377	0.847	1.789	0.476	1.072	2.264	0.310	0.698	1.473
	0.375	0.362	0.814	1.719	0.394	0.888	1.874	0.231	0.520	1.097
	0.500	0.341	0.767	1.619	0.324	0.730	1.541	0.168	0.377	0.796
	0.625	0.318	0.716	1.513	0.270	0.609	1.286	0.122	0.274	0.577
	0.750	0.299	0.673	1.420	0.234	0.526	1.111	0.089	0.201	0.424
	0.875	0.287	0.645	1.361	0.210	0.472	0.997	0.068	0.154	0.325
	1.000	0.281	0.633	1.336	0.201	0.453	0.957	0.062	0.139	0.292

Table 4 lists material properties, and Fig. 8 shows a schematic of the temperature distribution. Dashes replace stress-intensity factors in the boundary layer (see Section 6.3).

Acknowledgements

The authors gratefully acknowledge support for this work from the NASA Graduate Student Researchers Program (NGT 2-52271) and the NASA-Ames Engineering for Complex Systems Program (NAG 2-1424), for which NASA-Ames Chief Engineer Dr. Tina Panontin serves as the project technical monitor. Thanks are due also to the National Science Foundation (NSF) Mechanics and Materials Program (CMS-0115954). Any opinions, findings, and conclusions or recommendations expressed in this publication are those of the authors and do not necessarily reflect the views of the sponsors.

References

Anifantis, N.K., 2001. Crack surface interference: a finite element analysis. Engineering Fracture Mechanics 68 (12), 1403–1415.

Anderson, T.L., 1995. Fracture Mechanics, Fundamentals and Applications, second ed. CRC Press, New York.

Anlas, G., Santare, M.H., Lambros, J., 2000. Numerical calculation of stress intensity factors in functionally graded materials. International Journal of Fracture 104, 131–143.

Aoki, S., Kishimoto, K., Sakata, M., 1982. Elastic–plastic analysis of crack in thermally-loaded structures. Engineering Fracture Mechanics 16 (3), 405–413.

Ayhan, A.O., Nied, H.F., 2002. Stress intensity factors for three-dimensional surface cracks using enriched finite elements. International Journal for Numerical Methods in Engineering 54, 899–921.

Bahr, H.-A., Fischer, G., Weiss, H.-J., 1986. Thermal shock crack patterns explained by single and multiple crack propagation. Journal of Materials Science 21 (8), 2716–2720.

Bao, G., Cai, H., 1997. Delamination cracking in functionally graded coating/metal substrate systems. Acta Materiala 45 (3), 1055–1066.

Bazant, Z.P., Estenssoro, L.F., 1979. Surface singularity and crack propagation. International Journal of Solids and Structures 15, 405–426.

Benthem, J.P., 1977. State of stress at the vertex of a quarter-infinite crack in a half-space. International Journal of Solids and Structures 13, 479–492.

Bicanic, N., Hinton, E., 1979. Spurious modes in two-dimensional isoparametric elements. International Journal for Numerical Methods in Engineering 14 (10), 1545–1557.

Bruck, H.A., Gershon, A.L., 2002. Three-dimensional effects near the interface in a functionally graded Ni-Al203 plate specimen. International Journal of Solids and Structures 39, 547–557.

Cai, H., Bao, G., 1998. Crack bridging in functionally graded coatings. International Journal of Solids and Structures 35 (7–8), 701–717.

Chen, J., Wu, L., Du, S., 2000. A modified *J* integral for functionally graded materials. Mechanics Research Communications 27 (3), 301–306.

Chuntu, L., Yingzhi, L., 1987. Study on cracked plates, shells and three dimensional bodies. Engineering Fracture Mechanics 28 (5–6), 741–760.

Cook, R.D., Malkus, D.S., Plesha, M.E., Witt, R.J., 2002. Concepts and Applications of Finite Element Analysis, fourth ed. John Wiley and Sons, New York.

Dag, S., Kadioglu, S., Yahsi, O.S., 1999. Circumferential crack problem for an FGM cylinder under thermal stresses. Journal of Thermal Stresses 22, 659–687.

Delale, F., Erdogan, F., 1983. The crack problem for a nonhomogeneous plane. ASME Journal of Applied Mechanics 50, 609–614.

Dolbow, J.E., Gosz, M., 2002. On the computation of mixed-mode stress intensity factors in functionally graded materials. International Journal of Solids and Structures 39, 2557–2574.

Eischen, J.W., 1987. Fracture of nonhomogeneous materials. International Journal of Fracture 34, 3–22.

Erdogan, F., Wu, B.H., 1996. Crack problems in FGM layers under thermal stresses. Journal of Thermal Stresses 19, 237–265.

Erdogan, F., Wu, B.H., 1997. The surface crack problem for a plate with functionally graded properties. ASME Journal of Applied Mechanics 64, 449–456.

Eriksson, K., 2002. A domain independent integral expression for the crack extension force of a curved crack in three dimensions. Journal of the Mechanics and Physics of Solids 50, 381–403.

Frangi, A., 2002. Fracture propagation in 3D by the symmetric Galerkin boundary element method. International Journal of Fracture 116, 313–330.

Fujimoto, T., Noda, N., 2000. Crack propagation in a functionally graded plate under thermal shock. Archive of Applied Mechanics 70, 377–386.

Fujimoto, T., Noda, N., 2001. Influence of the compositional profile of functionally graded material on the crack path under thermal shock. Journal of the American Ceramic Society 84 (7), 1480–1486.

Gaudette, F.G., Giannakopoulos, A.E., Suresh, S., 2001. Interface cracks in layered materials subjected to a uniform temperature change. International Journal of Fracture 110 (4), 325–349.

Gu, P., Asaro, R.J., 1997. Cracks in functionally graded materials. International Journal of Solids and Structures 34 (1), 1–17.

Gu, P., Dao, M., Asaro, R.J., 1999. A simplified method for calculating the crack tip field of functionally graded materials using the domain integral. ASME Journal of Applied Mechanics 66, 101–108.

Gullerud, A.S., Koppenhoefer, K.C., Roy, A., Dodds Jr., R.H., 2000. WARP3D-Release 13.18 Manual. Civil Engineering, Report No. UILU-ENG-95-2012, University of Illinois at Urbana-Champaign, Urbana, IL.

Hartranft, R.J., Sih, G.C., 1969. The use of eigenfunction expansions in the general solution of three-dimensional crack problems. Journal of Mathematics and Mechanics 19, 123–138.

Hartranft, R.J., Sih, G.C., 1970. An approximate three-dimensional theory of plates with applications to crack problems. International Journal of Engineering Science 8, 711–729.

Hasselman, D.P.H., Youngblood, G.E., 1978. Enhanced thermal resistance of structural ceramics with thermal conductivity gradients. Journal of the American Ceramic Society 61, 49–52.

Jin, Z.H., Noda, N., 1994. Crack tip singular fields in nonhomogeneous materials. ASME Journal of Applied Mechanics 61 (3), 738–740.

Jin, Z.-H., Batra, R.C., 1996. Some basic fracture mechanics concepts in functionally graded materials. Journal of the Mechanics and Physics of Solids 44 (8), 1221–1235.

Jin, Z.-H., Batra, R.C., 1998. *R*-curve and strength behavior of a functionally graded material. Materials Science and Engineering A 242, 70–76.

Kawasaki, A., Watanabe, R. 1993. Fabrication of disk-shaped functionally graded materials by hot pressing and their thermomechanical performance. In: Holt, J.B., Koizumi, M., Hirai, T., Munir, Z.A. (Eds.), Proceedings of the Second International Symposium on Functionally Gradient Materials. American Ceramic Society, Westerville, OH, pp. 157–164.

Kim, J.H., Paulino, G.H., 2002a. Finite element evaluation of mixed mode stress intensity factors in functionally graded materials. International Journal for Numerical Methods in Engineering 53, 1903–1935.

Kim, J.H., Paulino, G.H., 2002b. Mixed-mode fracture of orthotropic functionally graded materials using finite elements and the modified crack closure method. Engineering Fracture Mechanics 69, 1557–1586.

Kim, J.H., Paulino, G.H., 2002c. Isoparametric graded finite elements for nonhomogeneous isotropic and orthotropic materials. ASME Journal of Applied Mechanics 69, 502–514.

Kim, J.H., Paulino, G.H., 2003. Mixed-mode *J*-integral formulation and implementation using graded elements for fracture analysis of nonhomogeneous orthotropic materials. Mechanics of Materials 35, 107–128.

Kim, Y.H., Jones, R.F., Lee, S.W., 1990. Study of 20-node solid element. Communications in Applied Numerical Methods 6 (3), 197–205.

Kokini, K., Takeuchi, Y.R., Choules, B.D., 1996. Thermal crack initiation mechanisms on the surface of functionally graded ceramic thermal barrier coatings. Ceramics International 22, 397–401.

Konda, N., Erdogan, F., 1994. The mixed-mode crack problem in a nonhomogeneous elastic medium. Engineering Fracture Mechanics 47, 533–545.

Lee, Y.-D., Erdogan, F., 1995. Residual/thermal stresses in FGM and laminated thermal barrier coatings. International Journal of Fracture 69, 145–165.

Lee, Y.-D., Erdogan, F., 1998. Interface cracking of FGM coatings under steady-state heat flow. Engineering Fracture Mechanics 59 (3), 361–380.

Li, C., Zou, Z., Duan, Z., 1999. Stress intensity factors for functionally graded solid cylinders. Engineering Fracture Mechanics 63, 735–749.

Li, C., Zou, Z., Duan, Z., 2000. Multiple isoparametric finite element method for nonhomogeneous media. Mechanics Research Communications 27 (2), 137–142.

Li, F.Z., Shih, C.F., Needleman, A., 1985. A comparison of methods for calculating energy release rates. Engineering Fracture Mechanics 21, 405–421.

Li, S., Mear, M.E., Xiao, L., 1998. Symmetric weak-form integral equation method for three-dimensional fracture analysis. Computer Methods in Applied Mechanics and Engineering 151, 435–459.

Marur, P.R., Tippur, H.V., 2000. Numerical analysis of crack-tip fields in functionally graded materials with a crack normal to the elastic gradient. International Journal of Solids and Structures 37, 5353–5370.

Merkle, J.G., 1973. A review of some of the existing stress intensity factor solutions for part-through surface cracks. ORNL-TM-3983, US Atomic Energy Commission.

Miyamoto, Y., Kaysser, W.A., Rabin, B.H., Kawasaki, A., Ford, A.G., 1999. Functionally Graded Materials: Design, Processing and Applications. Kluwer Academic Publishers, Boston.

Moran, B., Shih, C.F., 1987a. A general treatment of crack tip contour integrals. International Journal of Fracture 35, 295–310.

Moran, B., Shih, C.F., 1987b. Crack tip and associated domain integrals from momentum and energy balance. Engineering Fracture Mechanics 27 (6), 615–642.
Nakamura, T., Parks, D.M., 1988. Three-dimensional stress field near the crack front of a thin elastic plate. ASME Journal of Applied Mechanics 55, 805–813.
Nakamura, T., Parks, D.M., 1989. Antisymmetrical 3-D stress field near the crack front of a thin elastic plate. International Journal of Solids and Structures 25 (12), 1411–1426.
Narayana, K.B., George, S., Dattaguru, B., Ramamurthy, T.S., Vijayakumar, K., 1994. Modified crack closure integral (MCCI) for 3-d problems using 20-noded brick elements. Fatigue and Fracture or Engineering Materials and Structures 17 (2), 145–157.
Nemat-Nasser, S., Hori, M., 1993. Micromechanics: Overall Properties of Heterogeneous Materials. Elsevier, North-Holland.
Newman, J.C., Raju, I.S., 1979. Analyses of surface cracks in finite plates under tension or bending loads. NASA Technical Paper 1578.
Nikishkov, G.P., Atluri, S.N., 1987a. An equivalent domaina integral method for computing crack-tip integral parameters in non-elastic, thermomechanical fracture. Engineering Fracture Mechanics 26, 851–867.
Nikishkov, G.P., Atluri, S.N., 1987b. Calculation of fracture mechanics parameters for an arbitrary three-dimensional crack, by the 'equivalent domain integral' method. International Journal for Numerical Methods in Engineering 24, 1801–1821.
Noda, N., Jin, Z.-H., 1993. Thermal stress intensity factors for a crack in a strip of a functionally gradient material. International Journal of Solids and Structures 30, 1039–1056.
Noda, N., 1997. Thermal stresses intensity factor for functionally gradient plate with an edge crack. Journal of Thermal Stresses 20, 373–387.
Noda, N., 1999. Thermal stresses in functionally graded materials. Journal of Thermal Stresses 22 (1), 477–512.
Nomura, N., Gasik, M., Kawasaki, A., Watanabe, R., 2001. Thermomechanical modelling of functionally graded thermal barrier coatings. In: Proceedings of the 6th International Symposium on Functionally Graded Materials, vol. 114, pp. 223–229.
Pook, L.P., 1994. Some implications of corner point singularities. Engineering Fracture Mechanics 48 (3), 367–378.
Quian, G., Nakamura, T., Berndt, C.C., 1998. Effects of thermal gradient and residual stresses on thermal barrier coating fracture. Mechanics of Materials 27, 91–110.
Rajaram, H., Socrate, S., Parks, D.M., 2000. Application of domain integral methods using tetrahedral elements to the determination of stress intensity factors. Engineering Fracture Mechanics 66, 455–482.
Raju, I.S., Newman, J.C., 1979. Stress-intensity factors for a wide range of semi-elliptical surface cracks in finite-thickness plates. Engineering Fracture Mechanics 11, 817–829.
Raju, I.S., 1987. Calculation of strain-energy release rates with high order and singular finite elements. Engineering Fracture Mechanics 28 (3), 251–274.
Ramamurthy, T.S., Krishnamurthy, T., Narayana, K.B., Vijayakumar, K., Dataguru, B., 1986. Modified crack closure integral method with quarter point elements. Mechanics Research Communications 13 (4), 179–186.
Ravichandran, K.S., 1995. Thermal residual stresses in a functionally graded material system. Materials Science and Engineering A 201, 269–276.
Rice, J.R., 1968. A path-independent integral and the approximate analysis of strain concentration by notches and cracks. ASME Journal of Applied Mechanics 35, 379–386.
Rice, J.R., Levy, N., 1972. The part-through surface crack in an elastic plate. ASME Journal of Applied Mechanics 39 (1), 185–194.
Rice, J.R., Paris, P.C., Merkle, J.G., 1973. Some further results on J-integral analysis and estimates. In: Progress in Flaw Growth and Fracture Toughness Testing, ASTM STP 536, 231–245.
Rousseau, C.-E., Tippur, H.V., 2001. Influence of elastic gradient profiles on dynamically loaded functionally graded materials: Cracks along the gradient. International Journal of Solids and Structures 38, 7839–7856.
Rybicki, E.F., Kanninen, M.F., 1977. A finite element calculation of stress intensity factors by a modified crack closure integral. Engineering Fracture Mechanics 9, 931–938.
Santare, M.H., Lambros, J., 2000. Use of graded finite elements to model the behavior of nonhomogeneous materials. ASME Journal of Applied Mechanics 67, 819–822.
Selvadurai, A.P.S., 2000. The penny-shaped crack at a bonded plane with localized elastic nonhomogeneity. European Journal of Mechanics and Solids 19, 525–534.
Shih, C.F., deLorenzi, H.G., German, M.D., 1976. Crack extension modeling with singular quadratic isoparametric elements. International Journal of Fracture 12, 647–651.
Shih, C.F., Moran, B., Nakamura, T., 1986. Energy release rate along a three-dimensional crack front in a thermally stressed body. International Journal of Fracture 30, 79–102.
Shivakumar, K.N., Raju, I.S., 1992. An equivalent domain integral method for three-dimensional mixed-mode fracture problems. Engineering Fracture Mechanics 42 (6), 935–959.
Takahashi, H., Ishikawa, T., Okugawa, D., Hashida, T., 1993. Laser and plasma-ARC thermal shock/fatigue fracture evaluation procedure for functionally gradient materials. In: Thermal Shock and Tehmal Fatigue Behavior of Advanced Ceramics. Kluwer Academic Publishers, Dordrecht.

Tohgo, K., Sakaguchi, M., Ishii, H., 1996. Applicability of fracture mechanics in strength evaluation of functionally graded materials. JSME International Journal Series A 39 (4), 479–488.

Williamson, R.L., Rabin, B.H., 1992. Numerical modeling of residual stresses in Ni-Al_2O_3 gradient materials. In: Ceramic Transactions, Proceedings of the 2nd International Symposium on Functionally Gradient Materials. The American Ceramic Society, Westerville, OH.

Wilson, W.K., Yu, I.W., 1979. The use of the *J*-integral in thermal stress crack problems. International Journal of Fracture 15 (4), 377–387.

Yau, J.F., Wang, S.S., Corten, H.T., 1980. A mixed-mode crack analysis of isotropic solids using conservation laws of elasticity. ASME Journal of Applied Mechanics 47 (2), 335–341.